

I thank the reviewer for the constructive comments and suggestions. My response to the review can be found in the attached document.

**R:** Referee's comment

**A:** Author's response

### General

I have revised the manuscript according to the reviewers' comments. There is a new subsection in Section 2 describing the experiments. The descriptions of the DR-scaling and OPM have been updated and partly re-written. As requested by the reviewer, the impact of the revised precipitation on the SMB of the NPI is now discussed in Section 4.2 and further considered in all following sections. For better overview, the paragraph about the constrains of the hydrological cycle on the SMB has been moved to a new Section (4.3). In the course of the revision, two new figures (Fig. 4 and 5) have been added. Also, Table 1 shows the precipitation estimates from the DR-scaling experiments, now.

---

### DR-scaling

**R:** DR-scaling: it is still not clear to me how the vertical precipitation gradient is "optimized". Which function are you minimizing or looking for zeros using the Newton-Raphson algorithm (better known as Newton method)? I would very much recommend to perform this method with two drying ratios (0.45 and 0.6) to be able to compare systematically with the OPM.

**A:** I have expanded the paragraph about the DR-scaling and its optimization in the hope that the procedure is now more comprehensible. For better illustration, I have included the optimization equation. In addition, precipitation was estimated using both  $DRS_{0.45}$  and  $DRS_{0.60}$  (please note that I have introduced the abbreviations  $OPM_{0.45}$ ,  $OPM_{0.60}$ ,  $DRS_{0.45}$ , and  $DRS_{0.60}$  for the experiments in the new Section 2 (Experiments), now). The sentences anticipating the results from these experiments have been moved to the first paragraph of chapter 3.2. In this paragraph, among other things, the optimized lapse-rate and the precipitation estimate for the  $DRS_{0.60}$  estimation is now presented. Furthermore, Table 1 has been extended with the corresponding data.

---

### Linear orographic precipitation model

**R:** Some equation are shown now, but in my point of view they rather confuse than contribute. Several variables are not explained. If you want to show equations, I would very much prefer to see the two coupled advection equations for cloud water and hydrometeors. They contain the models essentials. Then you can describe the solution methods with words ( or equations if you prefer) and give the necessary references. You should comment on how the choice of every model parameter influences the results. For the second experiment I would recommend to only change the drying ratio to 0.6 and leave the other model parameters untouched in order to get a better idea about the influence of this parameter (then you could also avoid the word extreme scenario).

**A:** I have revised the description of the OPM (Section 2) and kept only the fundamental equations. The theoretical foundations and implementation of the model as well as in-depth sensitivity studies have been described in detail in a vast number of studies, e.g. Smith and Barstad (2004), Bartstad and Smith (2005), Jiang and Smith (2003), Jiang (2003), Smith and Evans (2007), Kunz and Kottmeier (2006) etc. I therefore refrain from repeating the fundamental equations here and refer to the changes made for this study. However, I agree with the reviewer that not all quantities have been explained in the necessary detail and have done so in this manuscript version.

As far as the fixing of the Brunt-Väisälä frequency and the sensitivity factor is concerned, I do not agree with the reviewer. This strategy would not be in line with the aim of this study. The aim was to create an 'extreme' (ensemble) scenario that reflects observed atmospheric conditions but does not occur in its frequency. To achieve this, these quantities were deliberately set to the 98th percentile to derive the highest possible precipitation estimate. As already mentioned above, the influence of the individual quantities has already been investigated in theoretical sensitivity studies.

## References:

- Barstad I and Smith RB (2005) *Evaluation of an orographic precipitation model*. J. Hydromet., 6(1), 85–99.
- Jiang Q (2003) *Moist dynamics and orographic precipitation*. Tellus A, 55(4), 301–316.
- Jiang Q and Smith RB (2003) *Cloud timescales and orographic precipitation*. J. Atmos. Sci., 60(13), 1543–1559.
- Kunz M and Kottmeier C (2006) *Orographic enhancement of precipitation over low mountain ranges. Part I: Model formulation and idealized simulations*. J. Appl. Meteorol. Climatol., 45(8), 1025–1040.
- Smith RB and Barstad I (2004) *A linear theory of orographic precipitation*. J. Atmos. Sci., 61(12), 1377–1391.
- Smith RB and Evans JP (2007) *Orographic precipitation and water vapor fractionation over the Southern Andes*. J. Hydromet., 8(1), 3–19.
- 

## Physical constraints on local precipitation

**R:** In this section I would like to see all modeled precipitation fields (Figure 3) to see the differences in precipitation distribution of the DR-scaling and OPM (similar as it was done in Weidemann 2013). Precipitation totals seem to be very similar between both methods (Table 1). And I would like to see an analysis (hopefully one or more figures) indicating which of the set-ups is reproducing best the station data and which are possible biases (a differentiated analysis of stations on the windward and leeward side of the icefields can indicate a lot about the models performance to simulate the process of orographic precipitation.)

**A:** I have added another figure (Fig. 4) now that shows the differences between OPM and DR-scaling (although I think this figure is not necessary since the DR-scaling reflects, per definition, the topography). The one to one comparison between simulations and observations is given in detail in Table S3 in the supplement. For sake of clarity, I have added a new Figure 5 visualizing the relation between observations and the outcome of the different experiments. The figure (and the provided statistics such as bias and rmse) clearly confirms that OPM<sub>0.45</sub> outperforms the OPM<sub>0.60</sub> simulation. Again, there are only three stations located west of the Patagonian Icefields which complicates an in-depth comparison. These stations are highlighted in Figure 5 to emphasize the windward and leeward performance.

---

## Consequences of revised precipitation estimates on the surface mass balance of the SPI

**R:** Again, since this is a regional assessment, you should include the consequences of your modeled precipitation fields for both icefields. There is a very clear relationship between accumulation and surface mass balance for NPI as well. See figure below and attached data.

**A:** Thank you very much for the dataset. I have extended the analysis and discussion to the NPI throughout the text accordingly.

# Revisiting extreme precipitation amounts over southern South America and implications for the Patagonian Icefields

Tobias Sauter<sup>1</sup>

5 <sup>1</sup>Climate System Research Group, Institute of Geography, Friedrich-Alexander-University Erlangen-Nürnberg (FAU), Germany

*Correspondence to:* Tobias Sauter (tobias.sauter@fau.de)

**Abstract.** Patagonia is thought to be one of the wettest regions on Earth, although available regional precipitation estimates vary considerably. This uncertainty complicates understanding and quantifying the observed environmental changes, such as glacier recession, biodiversity decline in fjord ecosystems and enhanced net primary production. The Patagonian Icefields, for example, are one of the largest contributors to sea-level rise outside the polar regions, and robust hydroclimatic projections are needed to understand and quantify current and future mass changes. The reported projections of precipitation from numerical modelling studies tend to overestimate those from in-situ determinations and the plausibility of these numbers have never been carefully scrutinised, despite the significance of this topic to our understanding of observed environmental changes. Here I use simple physical arguments and a linear model to test the plausibility of the current precipitation estimates and its impact on the Patagonian Icefields. The results show that environmental conditions required to sustain a mean precipitation amount exceeding  $6.09 \pm 0.64$  m yr<sup>-1</sup> are untenable according to the regional moisture flux. The revised precipitation values imply a significant reduction in surface mass balance of the Patagonian Icefields compared to previously reported values. This yields a new perspective on the response of Patagonia's glaciers to climate change and their sea-level contribution and might also help reduce uncertainties in the change of other precipitation-driven environmental phenomena.

## 1 Introduction

Patagonia's weather and climate are largely shaped by baroclinic eddies, which are characterized by the interaction of the planetary waves with the mean flow (Garreaud, 2009; Garreaud et al., 2013; Schneider et al., 2003; Vallis et al., 2014). The same mesoscale eddies efficiently transfer water vapor from the tropics poleward (Langhamer et al., 2018; Schneider et al., 2010; Trenberth et al., 2005), and regularly (every 9-12 days) trigger narrow filaments of water-vapor-rich bursts called atmospheric rivers. These features temporarily increase the vertical integrated water vapor content (IWV) in the Southern Hemisphere mid-latitudes by more than 200% (Durre et al., 2006; Waliser and Guan, 2017). More than half of all extreme precipitation events (above the 98th percentile) in Patagonia are associated with land-falling atmospheric rivers (Waliser and Guan, 2017). Given the tight coupling between atmospheric moisture transport and hydroclimatic response, changes in moisture transport mechanisms not only dominate the inter-annual and multi-decadal precipitation variability in Patagonia (Aguirre et al., 2018; Aravena and Luckman, 2009; Garreaud, 2007; Garreaud and Muñoz, 2005; Muñoz and Garreaud, 2005;

Sauter et al., 2009; Schneider and Gies, 2004; Viale and Garreaud, 2015; Weidemann et al., 2013, 2018a), but also dictate the fate of the ice masses in this region.

The Andes constitute an effective barrier to the impinging moist tropospheric air masses, forming one of the most extreme climatic divides found worldwide (Barrett et al., 2009; Garreaud, 2009; Garreaud et al., 2013; Rasmussen et al., 2007; Smith & Evans, 2007). The strong orographic influence on the precipitation distribution is evident from both remote sensing (Wentz et al., 1998) and terrestrial observations (Fig. 1). Despite observational uncertainty along the coast, two characteristic precipitation regions are apparent: (i) a maritime pre-cordillera region with annual precipitation exceeding 2-3 m w.e. (water equivalent), and (ii) a semi-arid rain-shadow region ( $< 0.5$  m w.e.) east of the main ridge that extends several thousand kilometres towards the South Atlantic. However, little is known about precipitation along the main ridge and, in particular, on the Patagonian Icefields. Current estimates from firn cores (Schwikowski et al., 2006; Shiraiwa et al., 2002), discharge measurements (Escobar, 1992) and numerical modelling (Bravo et al., 2019; Lenaerts et al., 2014; Mernild et al., 2017; Schaefer et al., 2013, 2015; Weidemann et al., 2018b) suggest average annual precipitation rates of 5 to 8 m w.e. yr<sup>-1</sup>, and of 7 to  $>10$  m w.e. yr<sup>-1</sup> for the Northern and Southern Patagonian Icefield (NPI, SPI), respectively (see Table 1). Extreme precipitation rates between 15 m w.e. yr<sup>-1</sup> (Mernild et al., 2017; Schaefer et al., 2013, 2015; Schwikowski et al., 2006) and 30 m w.e. yr<sup>-1</sup> are suspected at isolated locations (Lenaerts et al., 2014). If these precipitation magnitudes are realistic, it is likely that the SPI is one of the wettest – if not *the* wettest – places on earth.

The considerable uncertainty in precipitation amounts in Patagonia not only affects our current understanding of the local hydrological cycle, but also has profound impacts on studies concerned with fjord ecosystems (Landaeta et al., 2012), biological production in water columns (Aracena et al., 2011; Vargas et al., 2018), net primary production (Jobbágy et al., 2002), glacier mass balance (Escobar, 1992; Foresta et al., 2018; Lenaerts et al., 2014; Mernild et al., 2017; Schaefer et al., 2013, 2015; Schwikowski et al., 2006; Shiraiwa et al., 2002; Weidemann et al., 2018b; Willis et al., 2012) and its contribution to sea level rise (Braun et al., 2019a; Malz et al., 2018; Marzeion et al., 2012; Rignot et al., 2003). Reducing the plausible range of precipitation rates is a key step towards improved process understanding of such systems and offers new perspectives on future changes.

Here I use simple physical scaling arguments and a linear modelling approach to test the plausibility of the current precipitation estimates in central Patagonia (45°S-52°S). In particular, I address the question of whether the water vapor flux (WVF) from the tropics to the mid-latitudes by baroclinic eddies can sustain these extreme precipitation estimates. The assessment of the hypothesis relies on three fundamental assumptions: (i) The orographically induced precipitation is proportional to the incoming WVF which acts as the major moisture resource for the precipitation system. This implies that uncertainties in the incoming WVF directly impact the precipitation estimate. (ii) The terrain forced uplift and condensation of moist air masses is assumed to be the dominant precipitation formation process in central Patagonia. (iii) The atmospheric drying ratio (DR)

derived from observed isotope data is a valid measure for the cross-mountain fractionation of the WVF. Based on this assumption, the proposed methods are constrained by the DR to accurately reproduce the fraction of the water vapor flux removed by orographic precipitation.

5 After a description of the methods (Sec. 2), the moisture transport and its role on local precipitation formation in southern South America is explored in more detail (Sec. 3.1). The next chapter (Sec. 4) begins with the analysis-assessment of the precipitation estimates (Sec. 4.1) ~~available atmospheric soundings and compares them with remote sensing products and reanalysis data. Following this, the knowledge gained from the experiments on local precipitation formation (Sec. 3.2) and discusses~~ and its implications for the surface mass balance of the Patagonian Icefields of the SPI (Sec. ~~4.3.2~~3). We will further link the surface mass balance to the local hydrological cycle to understand the long-term evolution of the glaciers in this region (Sec. 4.3). ~~Following this section, the limitation and uncertaintyes of the proposed approach is discussed (Sec. 4.4.) will be discussed and critically reviewed (Section 3.4).~~ The last section provides a conclusion of the main findings.

## 2 Methodology

### DR-scaling (DRS)

15 To provide a first assessment of the magnitude of precipitation, mean precipitation is estimated along the western slopes of the Andes (45°-52°S and 73°-76°W) using a simple DR-scaling (DRS). The DR in Patagonia, defined as the fraction of the WVF removed by orographic precipitation, is known to be the highest (~0.45-0.5) worldwide (Mayr et al., 2018; Smith and Evans, 2007). The ratio is a characteristic measure for mountain ranges and is independent of the incoming WVF. WhenIf the WVF and the DR are known, one can estimate the mean homogeneous (uniform) precipitation amount. ~~As the WVF and the DR (here we use 0.45) are known from ERA-Interim data and isotope observations (Dec et al., 2011; Langhamer et al., 2018; Mayr et al., 2018; Smith and Evans, 2007), one can estimate the mean homogeneous (uniform) precipitation amount.~~ To add altitude-dependent precipitation variability, the amount was redistributed mass-consistently by optimizing the vertical precipitation gradient using a Newton-Raphson algorithm (Press et al., 2007). The lapse-rate optimization finds the roots of the function

$$F(\gamma) = \frac{(DR \cdot WVF)}{A} - \iint_D (P_0 + \gamma \cdot h) = 0, \quad (1)$$

25 with A [m<sup>2</sup>] the study domain area, P<sub>0</sub> [m] the background precipitation at sea level, γ [m m<sup>-1</sup>] the precipitation gradient and h [m] the terrain height. The first term on the right represents the potential precipitation resulting from the WVF [kg m<sup>-1</sup> s<sup>-1</sup>] and the DR [-]. The second term is the precipitation integrated over the domain D resulting from the linear interpolation. The precipitation at sea level, P<sub>0</sub>, was taken from the Global Precipitation Measurement (GPM) mission offshore of the Chilean coast (-3 m yr<sup>-1</sup>). The optimization resulted in a vertical precipitation gradient of -0.0563 % m<sup>-1</sup>, which represents a slightly

~~higher lapse rate than previously reported rate of  $-0.05\% \text{ m}^{-1}$  (Schaefer et al., 2013, 2015).~~ This interpolation via lapse-rate approach converts the entire specified WVF fraction into precipitation regardless of the saturation vapor deficit of the impinging air masses. However, orographic precipitation can only occur when the terrain forced uplift and cooling of air masses lead to water vapor condensation. To take this condition into account, only lower tropospheric (below 950 hPa) air masses are considered with a relative humidity equal to or exceeding 90% (Jarosch et al., 2012; Weidemann et al., 2013). The ~~DR-sealing~~DRS provides a first-order approximation but neglects heterogeneity and important processes such as airflow dynamics and cloud physics.

### **Linear orographic precipitation model (OPM)**

To account for these aspects, a set of realistic and extreme ensemble experiments has been designed using a linear orographic precipitation model (OPM), which represents many processes, such as condensation and hydrometeor conversion, using relative simple formulations for airflow dynamics and cloud physics (e.g. Garreaud et al., 2016; Jarosch et al., 2012; Smith and Barstad, 2004; Smith and Evans, 2007; Weidemann et al., 2018a). The model builds upon the original formulation of the linear orographic precipitation model (Barstad and Smith, 2005; Smith and Barstad, 2004), including a correction of the WVF downstream (Smith and Evans, 2007) and an optimization to enforce the model towards a given drying ratio. It solves two steady-state advection equations describing the change in the vertically integrated cloud water density and hydrometeors density. Cloud water is generated due to advection, condensation of water vapor by terrain forced uplift, conversion from cloud water to hydrometeors, and hydrometeor fallout. Mountain wave theory allows for the decay of the vertical velocity caused by tilting mountain waves, and consequently constrains the water vapor condensation rate. Assuming horizontal uniform background flow and properties (e.g. atmospheric stability), the orographic precipitation can be represented by a transfer function

$$\hat{P}(k, l) = \frac{C_w i \sigma \hat{h}(k, l)}{(1 - i m H_w)(1 + i \sigma \tau_c)(1 + i \sigma \tau_f)} \quad (2)$$

where  $C_w$  [-] is the uplift sensitivity factor which relates the vertical air motion to the condensation rate,  $i$  is the imaginary unit,  $\sigma = Uk + Vl$  is the intrinsic frequency where  $k$  and  $l$  are the horizontal wavenumbers,  $\hat{h}(k, l)$  is the Fourier transform of the terrain,  $m$  is the vertical wavenumber,  $H_w$  [m] is the water vapor scale height, and  $\tau_c$  and  $\tau_f$  [s] are the time scales for the conversion from cloud water to hydrometeors and their precipitation. The airflow dynamics is represented by the vertical wavenumber  $m$  which is a function of the atmospheric stratification represented by the moist Brunt Väisälä frequency  $N_m^2$  [ $\text{s}^{-1}$ ]. Thus, the parsimonious model contains five parameters, the uplift sensitivity factor  $C_w$ , the moist buoyancy frequency  $N_m^2$ , the water vapor scale height  $H_w$ , and the condensation and fallout time scales  $\tau_c$  and  $\tau_f$ . The mean horizontal wind velocities (U, V) and the parameters  $C_w$  and  $N_m^2$  are calculated from 6-hourly ERA-Interim fields (2010-2016) below the 500 hPa

geopotential level off Patagonia's west coast between 48°-52°S and 75°-78°W (Fig. 1, D1) (Smith and Barstad, 2004). On contrary to most other studies,  $H_w$  is directly derived from the incoming WVF using  $H_w = WVF/(\rho q_w U)$ , where  $q_w$  [kg kg<sup>-1</sup>] is the total mixing ratio and  $\rho$  [kg m<sup>-3</sup>] the air density. The time scales of  $\tau_c = \tau_f = 850$  s are fixed for all experiments, which are realistic values for Southern Andes and produce remarkable similar results to numerical models (Garreaud et al., 2016; Smith and Evans, 2007).

The total precipitation field in physical space

$$P(x, y) = \max \left[ \left( \iint \hat{P}(k, l) e^{i(kx+ly)} dk dl + P_\infty \right), 0 \right], \quad (36)$$

is finally obtained by double Fourier transform Eq. (2) and adding the synoptic scale background precipitation,  $P_\infty$  [m], followed by the truncation of negative values. The vertical wavenumber is defined by

For consistency,  $P_\infty$  the latter one is calculated by removing the orographic component from the ERA-Interim precipitation field (e.g. for details see Dee et al. (2011) and Jarosch et al. (2012)). To enforce the model towards a given drying ratio  $DR_{def}$ ,  $P_\infty$  background precipitation is scaled by a constant, so that the calculated DR corresponds to  $DR_{def}$ . The model is solved on a 90 m SRTM dataset, resampled at 1 km resolution (Jarvis et al., 2008).

## Experiments

The orographic precipitation model is used to conduct a suite of ensemble experiments with 40 ensemble members. The ensembles members account for the initial condition uncertainty in the wind direction and moisture content by randomly perturbing  $\mathbf{U}$  (5%),  $\mathbf{V}$  (5%), and  $\mathbf{H}_w$  (10%) around its mean value. In the first experiment, it was tested whether a composite of 'realistic' atmospheric ambient conditions (derived from the reanalysis data), the observed drying ratio of 0.45 (Mayr et al., 2018) and WVF provides the basis to sustain the precipitation estimates of previous studies. The second experiment delivers an 'extreme' scenario by fixing the drying ratio at a higher value of 0.6 and setting the uplift sensitivity factor ( $C_w = 0.004$ ) and moist stability frequency ( $N_m = 0.007$ ) to their 98th percentile values.

Within the scope of this study, two experiments each were performed with the DR scaling DRS and the OPM. In the first experiment it was tested whether a combination of 'realistic' atmospheric environmental conditions (derived from the reanalysis data), the observed drying ratio DR of 0.45 (Mayr et al., 2018) and WVF provides the basis to sustain the precipitation estimates of previous studies. The second experiment delivers an 'extreme' scenario by setting the DR drying ratio to a higher value of 0.6. In this OPM experiment, the buoyancy sensitivity factor ( $C_w=0.004$ ) and the moisture stability frequency ( $N_m=0.007 \text{ s}^{-1}$ ) were also set to their 98th percentile values. The "extreme scenario" thus represents atmospheric conditions that exist are found in nature, but whose occurrence is extremely rare. To obtain an upper limit of the precipitation

potential, we assume that this atmospheric situation conditions is present every day. Ensemble experiments were created with the OPM orographic precipitation model for both scenarios. Each ensemble comprises 40 ensemble members. The ensemble members consider the uncertainty of the initial state in wind direction and moisture content by randomly perturbing U (5 %), V (5 %) and  $H_w$  (10 %) around their mean value. For simplicity's sake, from here on the "realistic" simulations are marked with the index subscript 0.45 (DRS<sub>0.45</sub> and OPM<sub>0.45</sub>), while the "extreme" simulations are marked with the index subscript 0.60 (DRS<sub>0.60</sub> and OPM<sub>0.60</sub>).

### Atmospheric Simulations using the Weather Research and Forecast model (WRF)

To analyze the influence of nonlinear flow regimes on precipitation patterns, atmospheric simulations were performed with the Weather Research and Forecast (WRF) model, version 3.8.1. The model was configured with three one-way nested domains with a horizontal resolution of 12.5 km, 2.5 km and 500 m which were centered over the Southern Patagonian Icefields. The model configuration and parameterizations used in this study are shown in Table S4. To achieve the required resolution in the inner domain, the standard terrain data was replaced by NASA Shuttle Radar Topography Mission (SRTM) data (<http://www.cgiar-csi.org/data/srtm-90m-digital-elevation-database-v4-1>). Furthermore, the land use classification was updated with the ESA CCI data set (<https://www.esa-landcover-cci.org>). This way the glacier outlines could be improved significantly. The outermost domain was driven at its lateral boundaries by the ERA-Interim reanalysis dataset with a spatial resolution of  $0.75^\circ \times 0.75^\circ$  in longitude/latitude and a time interval of 6 hours. With the above setup, individual events were calculated with WRF. Each simulation had a spin-up of at least 12 hours.

## 3 Results and Discussion

### 3.1 Moisture transport

Observations of IWV and WVF are sparse in South America and limits the analysis of the moisture transport to a few locations (see Fig. 2). The only available soundings for the region are Puerto Montt (41.4347°S, 73.0975°W) on the Pacific coast and Punta Arenas (53.0033°S, 70.8450°W) located at the Strait of Magellan (Durre et al., 2006). Along the coast at the latitude of Puerto Montt, the average WVF in the period 1990-2017 was about  $165.52 \pm 48.51 \text{ kg m}^{-1} \text{ s}^{-1}$ . Land-falling atmospheric rivers temporarily amplify the WVF by more than  $400 \text{ kg m}^{-1} \text{ s}^{-1}$ . There is also clear evidence that enhanced atmospheric circulation during strong El Niño events (Ocean Niño Index  $> 1.5$ ) increase the moisture flux over several months (see Fig. 2, e.g. 1997/98). The El Niño signal is less pronounced in Punta Arenas. The atmospheric soundings show opposite linear long-term WVF trends over the period 1990-2016 with a significant ( $p < 0.08$ ) decrease of  $-4.46 \text{ kg m}^{-1} \text{ s}^{-1}$  ( $-2.70\%$ ) decade<sup>-1</sup> in Puerto Montt, and a significant ( $p < 0.05$ ) positive trend of  $8.79 \text{ kg m}^{-1} \text{ s}^{-1}$  ( $5.11\%$ ) decade<sup>-1</sup> in Punta Arenas (see Fig. 2). However, change-point analysis shows that the observed WVF trend in Punta Arenas is not constant over time, but has shown significant abrupt

shifts in the past that characterize the transition of water vapor rich and poor periods (Killick et al., 2012). A significant transition took place in 2006 which marks the beginning of a relative water vapor rich period (Fig. 2).

The ERA-Interim data, on which the analysis is based, reflects the interannual WVF variability and overall trend of the soundings but slightly overestimates the rate of change in Puerto Montt ( $-4.94 \text{ kg m}^{-1} \text{ s}^{-1} \text{ decade}^{-1}$ ,  $-4.43\% \text{ decade}^{-1}$ ), and underestimates the observed trend in Punta Arenas ( $4.10 \text{ kg m}^{-1} \text{ s}^{-1} \text{ decade}^{-1}$ ,  $2.70\% \text{ decade}^{-1}$ ). The mean WVF at both sites is weaker than the observed moisture transport. In Puerto Montt, the WVF is about  $111.54 \pm 34.40 \text{ kg m}^{-1} \text{ s}^{-1}$ , which is almost 30 % less than the estimate from the atmospheric sounding. The differences between observed WVF ( $172.12 \pm 54.19 \text{ kg m}^{-1} \text{ s}^{-1}$ ) and reanalysis data ( $152.08 \pm 57.08 \text{ kg m}^{-1} \text{ s}^{-1}$ ) is much lower in Punta Arenas. It is evident from the soundings that ERA-Interim data is too dry (according to the IWV) in the vicinity of Puerto Montt ( $-2.23 \text{ mm}$ ,  $-14.9\%$ ,  $p < 0.01$ ), and slightly too wet in the south ( $0.48 \text{ mm}$ ,  $4.6\%$ ,  $p < 0.05$ ) (see Fig. S2 and Table S2). The comparison with atmospheric water vapor data obtained by the Special Sensor Microwave Imager/Sounder (SSMIS) over the ocean confirms the north-south pattern (Wentz et al., 1998) (see supporting information Fig. S4). While IWV differences between ERA-Interim data and SSMIS south of  $45^\circ\text{S}$  are on average smaller than  $0.16 \text{ mm}$  ( $1.1\%$ ), larger deficits are apparent north of  $45^\circ\text{S}$  ( $< -0.8 \text{ mm}$ ).

Based on the comparison with the atmospheric soundings and SSMIS observation, ERA-Interim underestimates the IWV along the west coast of Patagonia (D1 in Fig. 1), where the corresponding parameters for the assessment were calculated, by less than 5%. However, comparison with the soundings suggests that the WVF in the ERA-Interim data along the west coast is weaker by 10-20% due to uncertainties in moisture advection. In the following analysis, a WVF bias of 10% is assumed and corrected accordingly.

### 3.2 Physical constraints on local precipitation

To obtain the plausible range of precipitation amounts in central Patagonia, the ~~DR-scaling~~DRS and the ~~linear model~~OPM are driven by the ERA-Interim data for the period 2010-2016. The DRS serves primarily intended to gain first-fundamental insights of into the order of magnitude of the the precipitation. -As the WVF and the DR (here we use 0.45) are known from ERA-Interim data and isotope observations (Dee et al., 2011; Langhamer et al., 2018; Mayr et al., 2018; Smith and Evans, 2007), one can estimate the mean homogeneous (uniform) precipitation amount using Eq. (1). The mean precipitation at sea level,  $P_0$  [m], was taken from the Global Precipitation Measurement (GPM) mission offshore of the Chilean coast ( $\sim 3 \text{ m yr}^{-1}$ ). Solving the optimization problem (see Eq. 1) The optimization resulted in a vertical precipitation gradient of  $\sim 0.056\% \text{ m}^{-1}$ , which is represents a slightly higher higher lapse rate than the previously reported lapse rate of  $\sim 0.05\% \text{ m}^{-1}$  (Schaefer et al., 2013, 2015). Averaged over the SPI and NPI, this approach produces values of  $4.67 \text{ m yr}^{-1}$  and  $4.94 \text{ m yr}^{-1}$ , respectively (see Fig. 1 and Table 1). The highest precipitation amounts are reached at the highest peakshest peaks on the NPIicefields receive precipitation with -amounts of up to  $9.68 \text{ m yr}^{-1}$ . To theoretically achieve an extremely high theoretical-DR of 0.6 ( $\text{DR}_{0.60}$ ), a

precipitation gradient of 0.12% is required. Such a strong gradient would lead to average precipitation amount of 8.45 m yr<sup>-1</sup> and 9.16 m yr<sup>-1</sup> on the SPI and NPI with maximum values of more than 20 m yr<sup>-1</sup>.

5 ~~The precipitation at sea level,  $P_0$ , was taken from the Global Precipitation Measurement (GPM) mission offshore of the Chilean coast ( $\sim 3$  m yr<sup>-1</sup>). The optimization resulted in a vertical precipitation gradient of  $-0.056\%$  m<sup>-1</sup>, which represents a slightly higher lapse rate than previously reported rate of  $-0.05\%$  m<sup>-1</sup> (Schaefer et al., 2013, 2015).~~

~~To further consider include simplified dynamical airflow processes in the estimation, albeit in simplified form, in the estimation we use the the OPM. The orographic precipitation model OPM is applied to a large domain (Fig. 1, D2) to avoid spurious numerical artefacts. The ensemble mean of the OPM<sub>0.45</sub> experiment (realistic experiment (DR=0.45) gives an average precipitation amount of 5.06±0.51 m yr<sup>-1</sup> over the SPI and 5.38±0.59 m yr<sup>-1</sup> over the NPI (Table 1, Fig. 3), indicating that the WVF can sustain relatively high mean precipitation amounts in Patagonia. However, precipitation estimates are up to 38% lower than estimates from previous numerical studies (Escobar, 1992; Lenaerts et al., 2014; Mernild et al., 2017; Schaefer et al., 2013, 2015; Schwikowski et al., 2006). The highest mean amounts are found in the highest regions on the western slopes of the icefields (SPI: 5.93±0.60 m yr<sup>-1</sup>; NPI: 5.83±0.64 m yr<sup>-1</sup>) and at the southernmost end of the SPI. The eastern slopes receive considerably less precipitation (SPI: 4.04±0.42 m yr<sup>-1</sup>; NPI: 4.37±0.48 m yr<sup>-1</sup>). Comparison with in-situ observations from the Dirección General de Aguas (DGA, Chile) indicates that the model slightly overestimates precipitation on the leeward side by 0.29±0.37 m yr<sup>-1</sup> (see Table S3). Higher deviations (1.07±1.30 m yr<sup>-1</sup>) occur at the stations on the west side which are located at the foot of the Patagonian Icefields. The overestimation is the result of the rapid increase in model terrain elevation and the absence of nonlinear processes in the linear model (see Sec. 3.4). The maximum precipitation amount (10.09±0.92 m yr<sup>-1</sup>), found on the SPI plateau, is 30–70% lower than previously simulated extremes (Lenaerts et al., 2014; Schaefer et al., 2013, 2015) and accumulation rates derived from an ice core (Shiraiwa et al., 2002). The large ensemble spread indicates that extreme precipitation is very sensitive to small uncertainties in ambient flow conditions (see Table 1). Even though the uncertainty in the background flow regime and dynamics may also be a possible origin of the extreme precipitation predicted by the mesoscale models, the responsible mechanisms explaining the significant differences remain unclear. It is likely that one reason is the model parameterization of processes. Some microphysical parameterization schemes are more ‘graupel-friendly’ than others, which can lead to strong hydrometeor formation. Since the choice of parameterization combinations can lead to very different results, each model must be examined individually. The sources are manifold and can only be speculative in the context of this study.~~

The OPM<sub>0.60</sub> extreme experiment (extreme) shows higher averaged precipitation amounts of 5.99±0.59 m yr<sup>-1</sup> and 6.09±0.64 m yr<sup>-1</sup> at the SPI and NPI, respectively (Fig. 3). The combination of short time scales, large drying ratio, strong moist stability frequency, and large uplift sensitivity factor increases the total precipitation and enhances the cross-mountain fractionation.

Despite the precipitation-enhancing parameter choices, the maximum precipitation ( $11.58 \pm 0.98 \text{ m yr}^{-1}$ ) represents a reduction of up to 60% compared to other numerical studies (Lenaerts et al., 2014; Schaefer et al., 2013, 2015). ~~In addition, the estimated maximum is presumably an overestimate itself, due to the 'extreme' parameter choice and to the exclusion of nonlinear effects, such as flow blocking (see Sec. 3.4), given the linear nature of the orographic model.~~

5

## 4 Discussion

### 4.1 Assessment of the precipitation estimates

Comparison with in-situ observations from the Dirección General de Aguas (DGA, Chile) indicates that the OPM<sub>0.45</sub> model slightly overestimates precipitation on the east side (leeward/downwind) side by  $0.29 \pm 0.37 \text{ m yr}^{-1}$  (see Fig. 5 and Table S3).

10 ~~HigherLarger deviations ( $1.07 \pm 1.30 \text{ m yr}^{-1}$ ) occur at the stations located at on the foot of the western slope west side which are located at the foot of the Patagonian Icefields. This number is somehow misleading as only three stations are available west of the Icefields. The overestimation is the result of the rapid increase in model terrain elevation and the absence of nonlinear processes in the linear model OPM (see Sec. 4.3.4.34). Please note that this number is somehow misleading as only three stations are available west of the Icefields. However,~~

15 ~~Considering~~On contrary to the simple DR-scaling, the OPM approach captures the observed quick drop in precipitation from west to east (see Fig. 4). ~~Taking all~~Taking all stations into account, the bias between the observations and simulation is about 0.42 m and with a the root mean squared error (rmseRMSE) of 0.70 m. If the three only three western stations stations west of the main ridge (Amalia, Puerto Eden, and Glaciar San Rafael) are ignoredneglectedignored, the bias is reduced to 0.27 m with a rmseRMSE of 0.44 m. The high coefficient of determination suggests that the annual variability is well represented.

20 ~~In the OPM<sub>0.60</sub> experiments, the bias (0.99 m) is significantly higher, indicating that the simulations are much more humid than the observationsto wet. , which is particularly evident again in the western locations. The high coefficients of determination suggestsuggest that the annual variability is well represented in the OPM<sub>0.45</sub> as well as in the OPM<sub>0.60</sub> experiments. In summary, both the temporal variability and the sharp spatial differentiation of precipitation areis well captured by the OPM<sub>0.45</sub> experiment. This OPM<sub>0.45</sub> result is therefore consistent with the in-situ observations while the OPM<sub>0.60</sub> result is too wet. At~~

25 ~~the same time i. It confirms the findings from the isotope measurements that the fractionation of the WVF is in the range of 0.45 (Mayr et al., 2018). The DR of 0.45 seems to be sufficient to adequately capture the observed precipitation at the stations, even if overall the mean annual precipitation is somewhat overestimated. Overall it can be concluded that the sharp spatial differentiation of precipitation is well captured by the OPM<sub>0.45</sub> experiment. The DR of 0.45 is sufficient to record the precipitation at the stations, even if the average annual precipitation is still slightly overestimated.~~

30

~~Studies come to very different precipitation totals on the main ridge of the Andes and often diverge even further when it comes to maximum precipitation. Studies conclude that precipitation levels in the area of the main Andean ridge vary considerably, and often diverge even further for maximum precipitation levels. Even if there are still big uncertainties about the average rainfalls at the main ridge of the Andes, the opinions about the extreme values often diverge much further.~~

5

~~The maximum precipitation amount of the OPM<sub>0.45</sub> experiment (10.09±0.92 m yr<sup>-1</sup>), found on the SPI plateau, is ~30-70 % lower than the previously simulated extremes maxima (Lenaerts et al., 2014; Schaefer et al., 2013, 2015) and the accumulation rates derived from an ice core (Shiraiwa et al., 2002). The values reported by these studies cannot even be achieved by the OPM<sub>0.60</sub> experiment and which are still~~

10

~~Neither can the values reported by these studies be achieved with the OPM<sub>0.60</sub> experiment, which are still 20-60 % lower (11.58±0.98 m yr<sup>-1</sup>). Please note, assuming a snow/rain ratio of 0.559 and a fresh snow density of 250 kg m<sup>-3</sup>; this would still result in a fresh snow accumulation of more than 257 m. Note that with a rain/snow ratio of 0.59 and a new snow density of 250 kg, such precipitation would lead to fresh snow accumulation of more than 27 m.~~

15

~~The large ensemble spread in maximum values indicates that extreme precipitation is very sensitive to small uncertainties in ambient flow conditions (see Table 1). Even though the uncertainty in the background flow regime and dynamics may also be a possible origin of the extreme precipitation predicted by the mesoscale models, the responsible mechanisms explaining the significant differences remain unclear. It is likely that one reason is the model parameterization of processes. Some microphysical parameterization schemes are more ‘graupel-friendly’ than others, which can lead to strong hydrometeor formation. Since the choice of parameterization combinations can lead to very different results, each model must be examined individually. The sources are manifold and can only be speculative in the context of this study.~~

20

~~Given the scarcity of data, especially at higher altitudes, estimates of extreme values are difficult to assess. Presumably, Presumable the~~

25

~~In addition, the estimated maximums are overestimated, presumably an overestimate itself, due to the ‘extreme’ parameter choice and to the exclusion of nonlinear effects, such as flow blocking (see Sec. 3.4), given the linear nature of the orographic model (see Section 4.43).~~

25

### **4.3.213 Consequences of revised precipitation estimates on the surface mass balance of the SPI Patagonian Icefields**

These revised precipitation estimates have critical implications for our current understanding of the response of Patagonia’s glaciers to climate change. Recent numerical studies (Mernild et al., 2017; Schaefer et al., 2015) suggest a mean annual surface mass gain of 1.78±0.36 m to 2.24 m w.e. yr<sup>-1</sup> for the SPI over recent decades, while surface mass balance (SMB) estimates for the NPI range between -0.16±0.73 m w.e. yr<sup>-1</sup> and 0.14±0.49 m w.e. yr<sup>-1</sup>. However, these assessments used mean precipitation rates well above (40-65%) the plausible range presented in this study.

30

To quantify the effect of the revised precipitation values on the SMB of the SPI, we use the significant linear relation ( $R^2=0.96$ ,  $p<0.05$ ) between ~~annual precipitation-snow accumulation sum~~ and ~~annual~~ SMB derived from Schaefer et al. (2015) (see Fig. 64), given by  $SMB=1.2588 \cdot P_s - 3.9355$ , where  $P_s$  [m] is the mean solid precipitation. The robustness of this relationship is indirectly proven by the study of- (Mernild et al. (2017)) ~~Mernild et al. (2016)~~, which is very close to the linear fitting line.

5 Taking into account the proposed solid to total precipitation ratio of 0.596 (Schaefer et al., 2015), the mean solid precipitation is  $3.02 \pm 0.30$  m w.e. (~~realistic scenario~~  $OPM_{0.45}$ ) and  $3.57 \pm 0.35$  m. w.e. (~~extreme scenario~~  $OPM_{0.60}$ ) for the SPI. Based on this assumption, the revised accumulation values would result in a mean SMB (2010-2016) between  $0.56 \pm 0.45$  m w.e.  $yr^{-1}$  ( $7.82 \pm 6.28$   $km^3$   $yr^{-1}$ , ~~extreme scenario~~  $OPM_{0.60}$ ) and  $-0.14 \pm 0.39$  m w.e.  $yr^{-1}$  ( $-1.95 \pm 5.45$   $km^3$   $yr^{-1}$ , ~~realistic scenario~~  $OPM_{0.45}$ ) on the SPI (Fig. 654). ~~The SMB estimate from the DR scaling is within these limits.~~

10 It appears that all mean SMB estimates are between the limits of the DRSR scaling values ( $DRS_{0.45}$ :  $-0.43$  m w.e.  $yr^{-1}$ ;  $DRS_{0.60}$ :  $1.79$  m w.e.  $yr^{-1}$ ).

Taking account of the recent geodetic mass balance observations ( $-0.941 \pm 0.19$  m w.e.) (Malz et al., 2018), the mean mass loss due to calving ranges between  $-1.5 \pm 0.64$  m. w.e.  $yr^{-1}$  ( $-20.95 \pm 8.94$   $km^3$   $yr^{-1}$ ) and  $-0.8 \pm 0.58$  m. w.e.  $yr^{-1}$  ( $-11.18 \pm 8.10$   $km^3$   $yr^{-1}$ ). The mean mass balance and calving flows derived here are subject to approach-related uncertainties and may deviate strongly from the values of individual years. A recently published study showed that calving fluxes at Jorge Montt Glacier fluctuated between  $1.16 \pm 0.66$   $km^3$   $yr^{-1}$  and  $3.81 \pm 1.10$   $km^3$   $yr^{-1}$  in the years 2012-2018 (Bown et al., 2019). Single ~~extreme~~ events cannot be represented with the approach presented here, since the mean SMB is used together with the geodetic mass balance observations which also constitutes an integrated value.

20 The same approach can be applied to the NPI to highlight the sensitivity of the SMB to the revised precipitation values. Using the accumulation and SMB data from Schaefer et al (2013), the linear relationship  $SMB=1.375 \cdot P_s - 5.713$  between snow accumulation and SMB is obtained. Here we use the same solid to total precipitation ratio, resulting in snow precipitation of  $3.20 \pm 0.35$  m w.e. ( $OPM_{0.45}$ ) and  $3.61 \pm 0.38$  m. w.e. ( $OPM_{0.60}$ ) for the NPI. When these values are inserted into the linear equation, the mean SMB is  $-0.72 \pm 0.52$  m w.e.  $yr^{-1}$  ( $-3.72 \pm 2.68$   $km^3$   $yr^{-1}$ ,  $OPM_{0.60}$ ) and  $-1.30 \pm 0.48$  m w.e.  $yr^{-1}$  ( $-6.72 \pm 2.48$   $km^3$   $yr^{-1}$ ,  $OPM_{0.45}$ ). Again, ~~t~~ The SMBs derived from the two DRS experiments define the outer limits between which all SMB estimates are located. Again,  $OPM_{0.45}$  and  $OPM_{0.60}$  experiments are between the limits of the DRS values ( $DRS_{0.45}$ :  $-1.66$  m w.e.  $yr^{-1}$ ;  $DRS_{0.60}$ :  $1.79$  m w.e.  $yr^{-1}$ ). Comparing the OPM experiments again with the geodetic mass balances (Braun et al., 2019b), reveal we find that the SMB of the  $OPM_{0.45}$  experiment is lower than the observation ( $-0.90 \pm 0.078$  m w.e.  $yr^{-1}$ ). This is an unphysical result which ~~can~~ might have two main reasons: (i) the revised precipitation estimates are too low, or (ii) the linear relationship between SMB and snow precipitation is unreliable. The first reason is difficult to verify, but ~~comparing~~ the comparison of the experiments with the stations consistently shows a positive bias. This reduces the probability that the experiments are too dry. The second argument is supported by the fact that the relationship between SMB and snow accumulation of Mernild et al. (2017) does not coincide with that of Schaefer et al (2013). The former shows more positive

SMB for the same accumulation (see Fig. 6). Let us assume for the sake of simplicity that there is a constant offset of  $-0.84 \text{ m w.e. yr}^{-1}$  according to which can be derived from the difference between the values provided by Mernild et al. (2017) and the linear relationship approximation. The corrected SMB estimates of the OPM<sub>0.45</sub> experiment would be shifted towards the range of  $-0.46 \pm 0.48 \text{ m w.e. yr}^{-1}$  and therefore be more positive than the geodetic mass balance. The corresponding mass loss by calving would be finally in the order of  $-0.44 \pm 0.55 \text{ m w.e. yr}^{-1}$  ( $-2.27 \pm 2.84 \text{ km}^3 \text{ yr}^{-1}$ ). This is a pure thought experiment and the numbers can only serve as orders of magnitude.

~~Let us assume for the sake of simplicity that this is a constant offset, the SMB estimates of the OPM<sub>0.45</sub> experiment would be in the range  $-0.46 \text{ m w.e. yr}^{-1}$  of OPM<sub>0.60</sub> and therefore more positive than the geodetic mass balance. If one puts the OPM<sub>0.60</sub> to ground, the corresponding a mass loss by calving of XXX kg results would be in the order of  $-0.44 \pm 0.59 \text{ m w.e. yr}^{-1}$  ( $-2.27 \pm 3.05 \text{ km}^3 \text{ yr}^{-1}$ ).~~  
 ~~$0.18 \pm 0.59 \text{ m w.e. yr}^{-1}$  ( $-0.93 \pm 3.05 \text{ km}^3 \text{ yr}^{-1}$ ).~~

Furthermore, an invariant and homogeneous liquid to solid precipitation ratio and a universal relationship between annual precipitation sums and SMB ~~has been~~ is assumed. Recently published studies indicate that the solid to liquid precipitation ratio vary locally (Bravo et al., 2019). Together with the snowdrift effect, which is also not considered here, this leads to large uncertainties in the mass change estimates (e.g. Sauter et al., 2013). However, this analysis clearly shows how sensitive the estimation of SMB and calving rates react to precipitation uncertainties.

~~Given the strong link between glacier SMB and the local hydrological cycle, the long term SMB evolution scales with the strength of the WVF, which is, in turn projected to increase in a warming climate. The WVF sensitivity along Patagonia's west coast ( $\sim 50^\circ\text{S}$ ) is on the order of  $\sim 15\% \text{ K}^{-1}$  ( $\sim 3\% \text{ decade}^{-1}$ ) as a result of the strengthening of the westerlies ( $\sim 20\% \text{ K}^{-1}$ ) and increase in IWV ( $\sim 5\% \text{ K}^{-1}$ ) south of  $45^\circ\text{S}$ . The latter is weaker than the change in global mean IWV which scales according to the Clausius Clapeyron relation ( $7\% \text{ K}^{-1}$ ) but is consistent with the assumption that increased latent heat flux is compensated by the sensible heat flux (Held et al., 2006; Schneider et al., 2010). The observed zonal wind trend is associated with a bias towards a more positive Southern Annular Mode (Garreaud et al., 2013; Marshall et al., 2017; Thompson & Solomon, 2002). The change of the WVF leads to stronger moisture flux convergence along the coastal zone west of the Andes main ridge. Ignoring the fact that the solid liquid ratio changes, which appears to be a reasonable assumption since temperature changes in the lower troposphere are negligible ( $\sim 0.01 \text{ K dec}^{-1}$ ), a mean mass gain of  $0.57 \pm 0.06 \text{ m w.e. per degree warming}$  ( $0.11 \pm 0.02 \text{ m w.e. decade}^{-1}$ ) is expected over the SPI. This rate is consistent with other studies (Mernild et al., 2017). Thus, although the precipitation values presented here indicate that present-day SMB of the SPI is likely not as positive as suggested by previous studies, SMB can be expected to show an increasing trend under continued warming conditions.~~

### 4.3 The effect of the WVF on SMB Constrains of the hydrological cycle on the SMB

Given the strong link between glacier SMB and the local hydrological cycle, the long-term SMB evolution scales with the strength of the WVF, which is, in turn projected to increase in a warming climate. The WVF sensitivity along Patagonia's west coast (~50°S) is on the order of ~15 % K<sup>-1</sup> (~3 % decade<sup>-1</sup>) as a result of the strengthening of the westerlies (~20 % K<sup>-1</sup>) and increase in IWV (~5 % K<sup>-1</sup>) south of 45°S. The latter is weaker than the change in global-mean IWV which scales according to the Clausius-Clapeyron relation (7 % K<sup>-1</sup>) but is consistent with the assumption that increased latent heat flux is compensated by the sensible heat flux (Held et al., 2006; Schneider et al., 2010). The observed zonal wind trend is associated with a bias towards a more positive Southern Annular Mode (Garreaud et al., 2013; Marshall et al., 2017; Thompson & Solomon, 2002). The change of the WVF leads to stronger moisture flux convergence along the coastal zone west of the Andes main ridge. Ignoring the fact that the solid-liquid ratio changes, which appears to be a reasonable assumption since temperature changes in the lower troposphere are negligible (~0.01 K dec<sup>-1</sup>), a mean mass gain of 0.57±0.06 m w.e. per degree warming (0.11±0.02 m w.e. decade<sup>-1</sup>) is expected over the SPI. This rate is consistent with other studies (Mernild et al., 2017). Thus, although the precipitation values presented here indicate that present-day SMB of the Patagonian Icefields SPI is likely not as positive as suggested by previous studies, SMB can be expected to show an increasing trend under continued warming conditions.

### 4.3.4 Limitations and nonlinearities

Given the linear nature of the approach used, the knowledge gained must be critically assessed and is only valid under certain conditions. This linear assumption requires a stably stratified atmospheric flow, more precisely given by a positive moist buoyancy frequency. During the study period from 2010 to 2016, the condition was fulfilled in more than 99% of all days. As a part of this assumption a linear mountain flow response is required, to guarantee that the airflow crosses the mountain range. To ensure a linear flow regime, the non-dimensional mountain height  $\hat{H} = (N_m h_m)/U$  must be smaller than one, where  $h_m$  [m] is the mean barrier height. Assuming a mean  $h_m = 2200$  m, the conditions ( $\hat{H} < 1$ ) is fulfilled in >82% of all considered cases (see Fig. S5). In the remaining cases ( $\hat{H} \geq 1$ ), the Andes block the atmospheric flow, and a northerly low-level barrier jet forms along the west slope, parallel to the main ridge (Barrett et al., 2009; Falvey and Garreaud, 2007; Garreaud and Muñoz, 2005; Viale and Garreaud, 2015) (see Fig. 765). The low-level jet constitutes an effective barrier to the flow that extends upwind, greatly reducing the uplift motions and thus the condensation of water vapor along the west slopes. The shift in the vertical uplift enhances precipitation upstream of the Andes, while reducing precipitation at the slopes. The effect of blocking is clearly evident in the precipitation fields of high-resolution (500 m) atmospheric simulations of single events using the Weather Research and Forecast (WRF) model (see Fig. 876 and Table S4). Two water-vapor-rich events were chosen to illustrate the influence of the flow regime on the spatial distribution of precipitation. While the linear flow regime has a pronounced precipitation maximum on the slopes, flow blocking shifts the precipitation far upstream (600-700 km) leading to a more homogeneous pattern.

Upstream precipitation can be further enhanced by microphysical processes such as the seeder-feeder mechanism and rapid warm air autoconversion. Studies have shown that these processes can lead to higher rain accumulations upstream when fronts and embedded atmospheric rivers intersect the west coast of central Chile (Garreaud et al., 2016; Massmann et al., 2017; Viale et al., 2013; Viale and Garreaud, 2015). The lifting of moist air masses upstream produces mid-tropospheric stratiform clouds (seeder) which can be strong enough to produce snow/graupel aloft and light precipitation in the pre-frontal region. If the frontal system is slowed down by blocking, low-level convergence enhances in the area of the narrow cold-frontal rainband and fuels the updrafts. The enhanced updrafts facilitate the development of low-level clouds by collision-coalescence between supercooled droplets. When the narrow cold frontal rainband propagates further east it triggers the seeder-feeder mechanism and low-tropospheric clouds are seeded by the precipitation that is formed by mid-tropospheric clouds aloft. The associated rapid transformation of cloud water into hydrometeors and increased hydrometeor sizes are absent in the approach presented. Here, the process is treated simplistic by the choice of small time scales and by constraining the synoptic-scale uplift (background precipitation). This solution most likely lead to (i) an overestimation of precipitation on the west slopes of the SPI, (ii) an underestimation of precipitation in the Pre-Cordillera zone, but (iii) satisfies the given  $DR_{def}$  constraint. Compliance with the DR criterion is the necessary condition to verify the plausibility of precipitation estimates.

## 5.4 Conclusion

The present study has shown on the basis of simple physical arguments and a linear model that it is very unlikely that the moisture flux from the Pacific will be sufficient to sustain the reported extreme mean precipitation amounts for Patagonia. While the approaches and assumptions employed in this study contain substantial uncertainties, precipitation estimates using other parameter combinations fall within the range between the ~~realistic and the extreme~~ two proposed scenarios. Hence, this study offers a plausible range of precipitation estimates based on clearly defined assumptions: (i) the orographically induced precipitation is proportional to the incoming WVF, (ii) the terrain forced uplift and condensation of moist air masses is assumed to be the dominant precipitation formation process in central Patagonia, and (iii) the atmospheric drying ratio (DR) derived from observed isotope data is a valid measure for the cross-mountain fractionation of the WVF. According to these assumptions, the icefield-wide precipitation averages are likely to fall within  $5.06 \pm 0.51$  m w.e.  $yr^{-1}$  and  $5.99 \pm 0.59$  m w.e.  $yr^{-1}$  on the SPI, and  $5.38 \pm 0.59$  m w.e.  $yr^{-1}$  and  $6.09 \pm 0.64$  m w.e.  $yr^{-1}$  on the NPI. The ~~icefield-wide average~~ values within these ranges are about 40-65% lower than previously assumed. Extreme precipitation in wind-exposed regions is in the range of  $11.58 \pm 0.98$  m  $yr^{-1}$ , up to 60% lower than estimated by other numerical studies (Lenaerts et al., 2014; Schaefer et al., 2013, 2015). It should also be noted that processes such as snowdrift and nonlinear effects have not been taken into account so that the actual accumulation rates are probably still below these estimates. This result makes it very unlikely that Patagonia is the wettest place on Earth. More importantly, the drier hydroclimatic condition represents a major constraint for the Patagonian Icefields and reduces the precipitation contribution to the glacier mass balance. The missing contribution is evident in the

surface mass balance. According to the results, the average SMB (2010-2016) was between  $0.56 \pm 0.45$  m w.e.  $\text{yr}^{-1}$  ( $7.82 \pm 6.28$   $\text{km}^{-3} \text{yr}^{-1}$ ) and  $-0.14 \pm 0.39$  m w.e.  $\text{yr}^{-1}$  ( $-1.95 \pm 5.45$   $\text{km}^{-3} \text{yr}^{-1}$ ) on the SPI in the last decades. The mass loss due to calving ranged between  $-1.5 \pm 0.64$  m w.e.  $\text{yr}^{-1}$  ( $-20.95 \pm 8.94$   $\text{km}^{-3} \text{yr}^{-1}$ ) and  $-0.8 \pm 0.58$  m w.e.  $\text{yr}^{-1}$  ( $-11.18 \pm 8.10$   $\text{km}^{-3} \text{yr}^{-1}$ ). The SMB on the NPI the SMB was more negative with  $-0.72 \pm 0.52$  m w.e.  $\text{yr}^{-1}$  ( $-3.72 \pm 2.68$   $\text{km}^{-3} \text{yr}^{-1}$ ) and  $-1.30 \pm 0.48$  m w.e.  $\text{yr}^{-1}$  ( $-6.72 \pm 2.48$   $\text{km}^{-3} \text{yr}^{-1}$ ). The calving flux was estimated to be in the order of  $-0.44 \pm 0.55$  m w.e.  $\text{yr}^{-1}$  ( $-2.27 \pm 2.84$   $\text{km}^{-3} \text{yr}^{-1}$ ). However, this number is very uncertain. On the long-term, the regional precipitation is likely to increase by  $\sim 15\%$  per degree warming ( $\sim 3\%$   $\text{decade}^{-1}$ ) in response to stronger moisture flux. Most of the change is related to a strengthening of the westerlies ( $\sim 20\%$   $\text{K}^{-1}$ ), while only a minor contribution comes from an increase in IWV ( $\sim 5\%$   $\text{K}^{-1}$ ). Assuming that the liquid to solid precipitation ratio and the relationship between annual precipitation sum and SMB are universal and valid for the next decades, the WVF changes would result in a glacier surface mass gain of about  $0.57 \pm 0.06$  m w.e. per degree warming on the SPI. This positive trend contradicts the recently published geodetic mass balance observations (Malz et al., 2018), which detected quick glacier recessions in these regions. The observed retreat is significantly stronger than the gain in ice mass implying that the ice mass budget is partially decoupled from the climate signal and primarily caused by dynamic adjustments of tidewater and lake calving glaciers. The pronounced dynamic glacier response emphasizes that ice dynamic processes need to be given more prominence in order to quantify the response of the Patagonian glaciers to climate change and their contribution to future sea-level rise. While the change in ice masses is a vivid example of the response to reduced precipitation, it also opens new perspectives for future studies on environmental change in Patagonia and can also help reduce uncertainties in the quantification of other precipitation-driven environmental phenomena.

### Acknowledgments, Samples, and Data

This work was supported by the German Research Foundation (DFG), no. SA 2339/4-1. I would like to thank Manuel Gebetsberger, Emily Collier, Thomas Mölg, and Nicolas Cullen for the discussion and support. The simulations were calculated on the High-Performance Cluster (HPC) at the Regional Computation Center (RRZE) of the University of Erlangen-Nürnberg.

Data and materials availability: Data were obtained from the European Centre for Medium-Range Forecast (ECMWF), the National Aeronautics and Space Administration (NASA), Consortium for Spatial Information (CGIAR-CSI), and Integrated Global Radiosonde Archive (IGRA) from the National Centers for Environmental Information (NCEI). SSM/I and SSMIS data are produced by Remote Sensing Systems. Data are available at [www.remss.com/missions/ssmi](http://www.remss.com/missions/ssmi).

### References

Aguirre, F., Carrasco, J., Sauter, T., Schneider, C., Gaete, K. R., Garin, E., Adaros, R., Jaña, R. A. and Casassa, G.: Snow

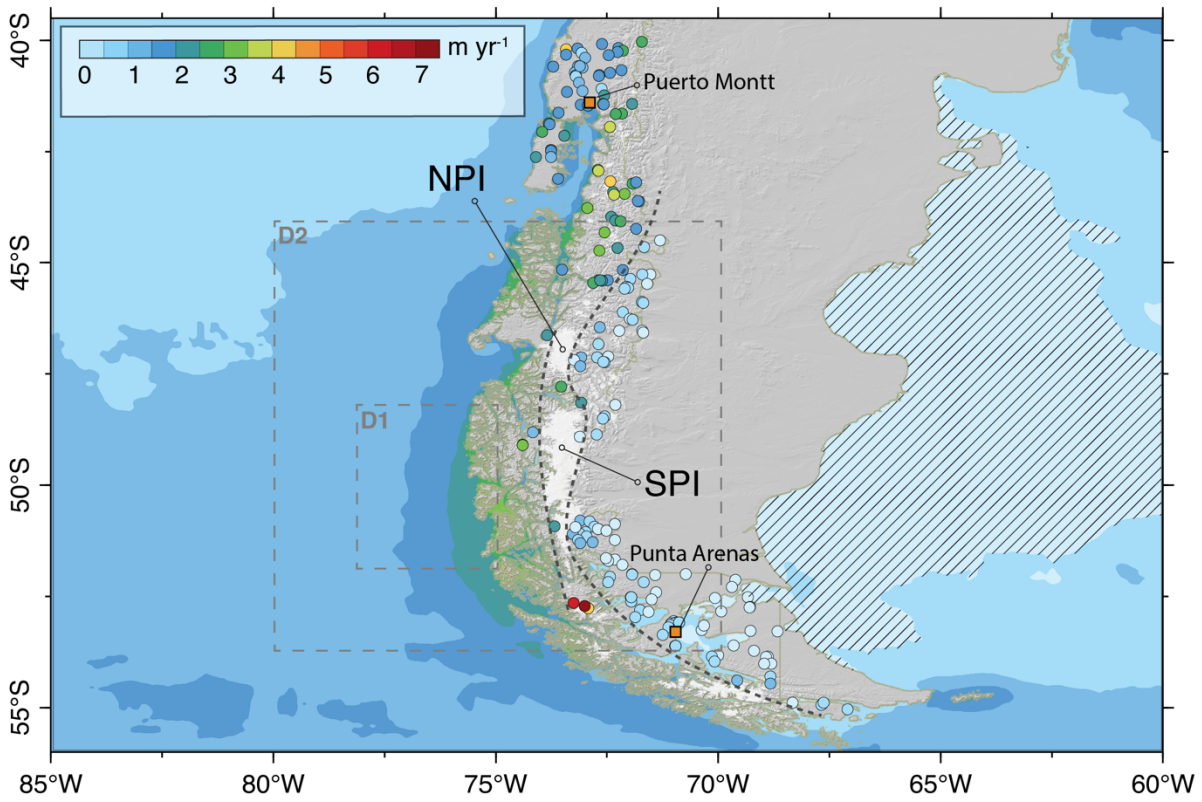
- cover change as a climate indicator in Brunswick Peninsula, Patagonia, *Front. Earth Sci.*, 6, 130, doi:<https://www.frontiersin.org/articles/10.3389/feart.2018.00130/abstract>, 2018.
- Aracena, C., Lange, C. B., Iriarte, J. L., Rebolledo, L. and Pantoja, S.: Latitudinal patterns of export production recorded in surface sediments of the Chilean Patagonian fjords (41-55 S) as a response to water column productivity, *Cont. Shelf Res.*, 5 31(3-4), 340-355, 2011.
- Aravena, J. C. and Luckman, B. H.: Spatio-temporal rainfall patterns in Southern South America, *Int. J. Climatol.*, 29, 2106-2120, doi:10.1002/joc, 2009.
- Barrett, B. S., Garreaud, R. and Falvey, M.: Effect of the Andes Cordillera on Precipitation from a Midlatitude Cold Front, *Mon. Weather Rev.*, 137(9), 3092-3109, doi:10.1175/2009MWR2881.1, 2009.
- 10 Barstad, I. and Smith, R. B.: Evaluation of an orographic precipitation model, *J. Hydrometeorol.*, doi:10.1175/JHM-404.1, 2005.
- Bown, F., Rivera, A., Pełlicki, M., Bravo, C., Oberreuter, J. and Moffat, C.: Recent ice dynamics and mass balance of Jorge Montt Glacier, Southern Patagonia Icefield, *J. Glaciol.*, 65(253), 732-744, doi:10.1017/jog.2019.47, 2019.
- Braun, M. H., Malz, P., Sommer, C., Farías-Barahona, D., Sauter, T., Casassa, G., Soruco, A., Skvarca, P. and Seehaus, T. C.: 15 Constraining glacier elevation and mass changes in South America, *Nat. Clim. Chang.*, 9(2), 130-136, doi:10.1038/s41558-018-0375-7, 2019.
- Bravo, C., Bozkurt, D., Gonzalez-Reyes, Á., Quincey, D. J., Ross, A. N., Farías-Barahona, D. and Rojas, M.: Assessing Snow Accumulation Patterns and Changes on the Patagonian Icefields, *Front. Environ. Sci.*, 7, 30, doi:10.3389/fenvs.2019.00030, 2019.
- 20 Dee, D. P., Uppala, S. M., Simmons, A. J., Berrisford, P., Poli, P., Kobayashi, S., Andrae, U., Balmaseda, M. A., Balsamo, G., Bauer, P., Bechtold, P., Beljaars, A. C. M., van de Berg, L., Bidlot, J., Bormann, N., Delsol, C., Dragani, R., Fuentes, M., Geer, A. J., Haimberger, L., Healy, S. B., Hersbach, H., Hólm, E. V., Isaksen, L., Kållberg, P., Köhler, M., Matricardi, M., McNally, A. P., Monge-Sanz, B. M., Morcrette, J. J., Park, B. K., Peubey, C., de Rosnay, P., Tavolato, C., Thépaut, J. N. and Vitart, F.: The ERA-Interim reanalysis: Configuration and performance of the data assimilation system, *Q. J. R. Meteorol. Soc.*, 137(656), 553-597, doi:10.1002/qj.828, 2011.
- 25 Durre, I., Vose, R. S. and Wuertz, D. B.: Overview of the integrated global radiosonde archive, *J. Clim.*, 19(1), 53-68, doi:10.1175/JCLI3594.1, 2006.
- Escobar, F.: Water balance in the Patagonia Icefield, *Glaciol. Res. Patagon.* 1990, 109-119, 1992.
- Falvey, M. and Garreaud, R.: Wintertime Precipitation Episodes in Central Chile: Associated Meteorological Conditions and 30 Orographic Influences, *J. Hydrometeorol.*, 8(2), 171-193, doi:10.1175/JHM562.1, 2007.
- Foresta, L., Gourmelen, N., Weissgerber, F., Nienow, P., Williams, J. J., Shepherd, A., Drinkwater, M. R. and Plummer, S.: Heterogeneous and rapid ice loss over the Patagonian Ice Fields revealed by CryoSat-2 swath radar altimetry, *Remote Sens. Environ.*, 211, 441-455, 2018.
- Garreaud, R., Falvey, M., Montecinos, A., Garreaud, R., Falvey, M. and Montecinos, A.: Orographic Precipitation in Coastal

- Southern Chile: Mean Distribution, Temporal Variability, and Linear Contribution, *J. Hydrometeorol.*, 17(4), 1185–1202, doi:10.1175/JHM-D-15-0170.1, 2016.
- Garreaud, R. D.: Precipitation and circulation covariability in the extratropics, *J. Clim.*, 20(18), 4789–4797, doi:10.1175/JCLI4257.1, 2007.
- 5 Garreaud, R. D.: The Andes climate and weather, *Adv. Geosci.*, 22, 3–11, doi:10.5194/adgeo-22-3-2009, 2009.
- Garreaud, R. D. and Muñoz, R. C.: The Low-Level Jet off the West Coast of Subtropical South America: Structure and Variability, *Mon. Weather Rev.*, 133(12), 2246–2261, doi:10.1175/MWR3074.1, 2005.
- Garreaud, R. D., Lopez, P., Minvielle, M. and Rojas, M.: Large-scale control on the Patagonian climate, *J. Clim.*, 26(1), 215–230, doi:10.1175/JCLI-D-12-00001.1, 2013.
- 10 Held, I. M., Soden, B. J., Held, I. M. and Soden, B. J.: Robust Responses of the Hydrological Cycle to Global Warming, *J. Clim.*, 19(21), 5686–5699, doi:10.1175/JCLI3990.1, 2006.
- Jarosch, A. H., Anslow, F. S. and Clarke, G. K. C.: High-resolution precipitation and temperature downscaling for glacier models, *Clim. Dyn.*, 38(1–2), 391–409, doi:10.1007/s00382-010-0949-1, 2012.
- Jarvis, A., Reuter, H. I., Nelson, A. and Guevara, E.: Hole-filled SRTM for the globe Version 4, 2008.
- 15 Jobbágy, E. G., Sala, O. E. and Paruelo, J. M.: Patterns and controls of primary production in the Patagonian steppe: a remote sensing approach, *Ecology*, 83(2), 307–319, 2002.
- Killick, R., Fearnhead, P. and Eckley, I. A.: Optimal detection of changepoints with a linear computational cost, *J. Am. Stat. Assoc.*, 107(500), 1590–1598, doi:10.1080/01621459.2012.737745, 2012.
- Landaeta, M. F., López, G., Suárez-Donoso, N., Bustos, C. A., Balbontín, F. and Balbontín, F.: Larval fish distribution, growth and feeding in Patagonian fjords: potential effects of freshwater discharge, *Environ. Biol. Fishes*, 93(1), 73–87, doi:10.1007/s10641-011-9891-2, 2012.
- 20 Langhamer, L., Sauter, T. and Mayr, G. J.: Lagrangian Detection of Moisture Sources for the Southern Patagonia Icefield (1979–2017), *Front. Earth Sci.*, 6, 219, doi:10.3389/feart.2018.00219, 2018.
- Lenaerts, J. T. M., Van Den Broeke, M. R., van Wessem, J. M., van de Berg, W. J., van Meijgaard, E., van Uft, L. H., Schaefer, M. and Bilt, D.: Extreme precipitation and climate gradients in Patagonia revealed by high-resolution regional atmospheric climate modeling, *J. Clim.*, 27(12), 4607–4621, doi:10.1175/JCLI-D-13-00579.1, 2014.
- 25 Malz, P., Meier, W., Casassa, G., Jaña, R., Skvarca, P. and Braun, M. H.: Elevation and mass changes of the Southern Patagonia Icefield derived from TanDEM-X and SRTM Data, *Remote Sens.*, 10(2), 188, 2018.
- Marshall, G. J., Thompson, D. W. J. and van den Broeke, M. R.: The Signature of Southern Hemisphere Atmospheric Circulation Patterns in Antarctic Precipitation, *Geophys. Res. Lett.*, 44(22), 11,580–11,589, doi:10.1002/2017GL075998, 2017.
- 30 Marzeion, B., Jarosch, A. H. and Hofer, M.: Past and future sea-level change from the surface mass balance of glaciers, *Cryosph.*, 6(6), 1295–1322, 2012.
- Massmann, A. K., Minder, J. R., Garreaud, R. D., Kingsmill, D. E., Valenzuela, R. A., Montecinos, A., Fulst, S. L. and Snider,

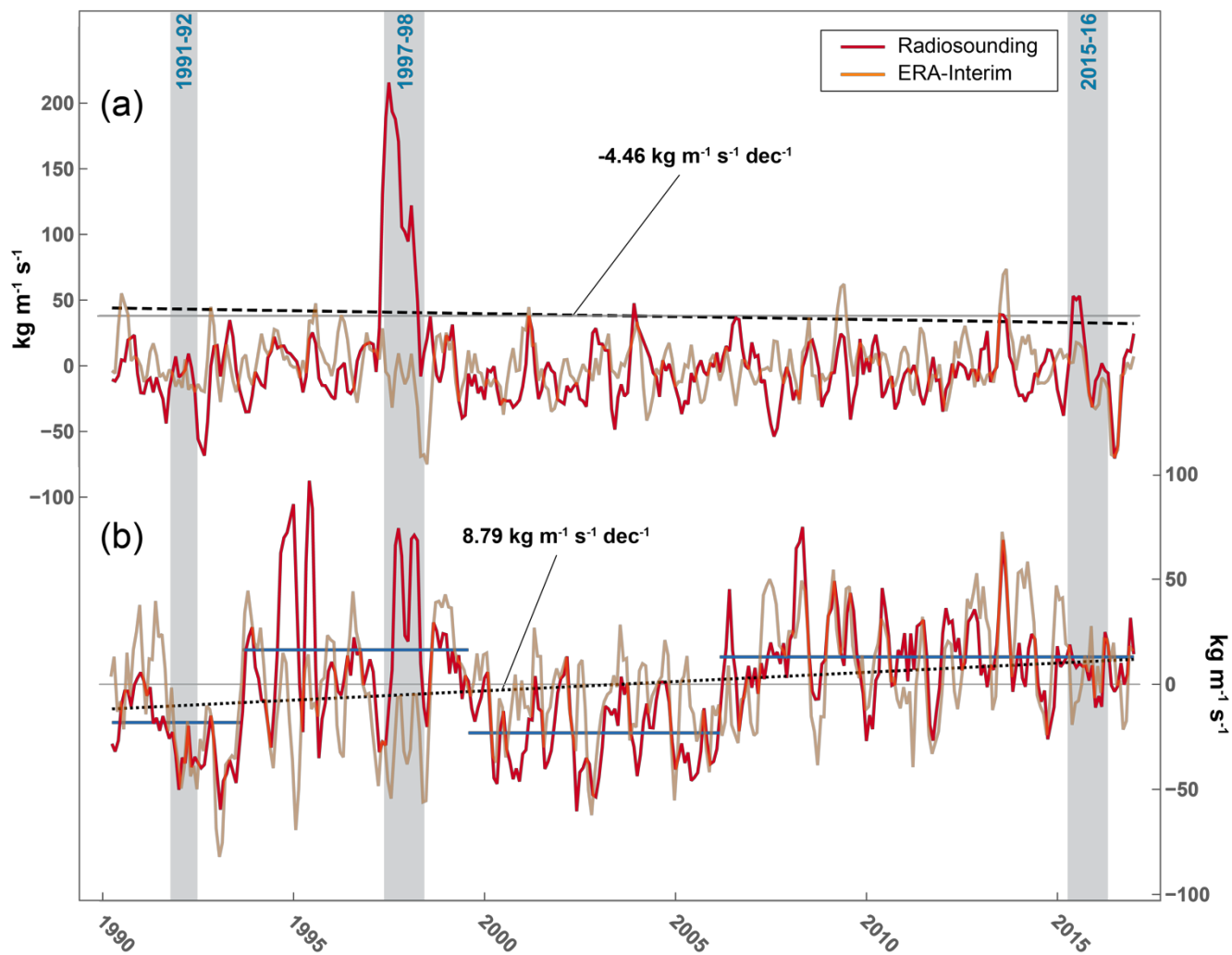
- J. R.: The Chilean Coastal Orographic Precipitation Experiment: Observing the Influence of Microphysical Rain Regimes on Coastal Orographic Precipitation, *J. Hydrometeorol.*, 18(10), 2723–2743, doi:10.1175/jhm-d-17-0005.1, 2017.
- Mayr, C., Langhamer, L., Wissel, H., Meier, W., Sauter, T., Laprida, C., Massafiero, J., Försterra, G. and Lücke, A.: Atmospheric controls on hydrogen and oxygen isotope composition of meteoric and surface waters in Patagonia, *Hydrol. Earth Syst. Sci. Discuss.*, 1–22, doi:10.5194/hess-2018-431, 2018.
- Mernild, S. H., Liston, G. E., Hiemstra, C. and Wilson, R.: The Andes Cordillera. Part III: glacier surface mass balance and contribution to sea level rise (1979–2014), *Int. J. Climatol.*, 37(7), 3154–3174, doi:10.1002/joc.4907, 2017.
- Muñoz, R. C. and Garreaud, R. D.: Dynamics of the Low-Level Jet off the West Coast of Subtropical South America, *Mon. Weather Rev.*, 133(12), 3661–3677, 2005.
- 10 Press, W. H., Teukolsky, S. A., Vetterling, W. T. and Flannery, B. P.: Numerical recipes 3rd edition: The art of scientific computing, Cambridge university press., 2007.
- Rasmussen, L. A., Conway, H. and Raymond, C. F.: Influence of upper air conditions on the Patagonia icefields, , 59, 203–216, doi:10.1016/j.gloplacha.2006.11.025, 2007.
- Rignot, E., Rivera, A. and Casassa, G.: Contribution of the Patagonia Icefields of South America to Sea Level Rise, *Science* (80-. ), 302(5644), 434–437, doi:10.1126/science.1087393, 2003.
- 15 Sauter, T., Schneider, C., Kilian, R. and Moritz, M.: Simulation and analysis of runoff from a partly glaciated meso-scale catchment area in Patagonia using an artificial neural network, *Hydrol. Process.*, 23(7), 1019–1030, doi:10.1002/hyp.7210, 2009.
- Sauter, T., Möller, M., Finkelnburg, R., Grabiec, M., Scherer, D. and Schneider, C.: Snowdrift modelling for the vestfonna ice cap, north-eastern Svalbard, *Cryosphere*, 7(4), doi:10.5194/tc-7-1287-2013, 2013.
- 20 Schaefer, M., Machguth, H., Falvey, M. and Casassa, G.: Modeling past and future surface mass balance of the Northern Patagonia Icefield, *J. Geophys. Res. Earth Surf.*, 118(2), 571–588, doi:10.1002/jgrf.20038, 2013.
- Schaefer, M., MacHguth, H., Falvey, M., Casassa, G. and Rignot, E.: Quantifying mass balance processes on the Southern Patagonia Icefield, *Cryosphere*, 9(1), 25–35, doi:10.5194/tc-9-25-2015, 2015.
- 25 Schneider, C. and Gies, D.: Effects of El Niño-southern oscillation on southernmost South America precipitation at 53°S revealed from NCEP-NCAR reanalyses and weather station data, *Int. J. Climatol.*, 24(9), 1057–1076, doi:10.1002/joc.1057, 2004.
- Schneider, C., Glaser, M., Kilian, R., Santana, A., Butorovic, N. and Casassa, G.: Weather Observations Across the Southern Andes at 53°S, *Phys. Geogr.*, 24(2), 97–119, doi:10.2747/0272-3646.24.2.97, 2003.
- 30 Schneider, T., O’Gorman, P. a., Levine, X. J., Gorman, P. A. O. and Levine, X. J.: Water vapor and the dynamics of climate changes, *Rev. Geophys.*, (48), 1–22, doi:10.1029/2009RG000302.1.INTRODUCTION, 2010.
- Schwikowski, M., Brüttsch, S., Casassa, G. and Rivera, A.: A potential high-elevation ice-core site at Hielo Patagónico Sur, *Ann. Glaciol.*, 43, 8–13, 2006.
- Shiraiwa, T., Kohshima, S., Uemura, R., Yoshida, N., Matoba, S., Uetake, J. and Godoi, M. A.: High net accumulation rates

- at Campo de Hielo Patagonico Sur, South America, revealed by analysis of a 45.97 m long ice core, *Ann. Glaciol.*, 35(1), 84–90, 2002.
- Smith, R. B. and Barstad, I.: A Linear Theory of Orographic Precipitation, *J. Atmos. Sci.*, 61(12), 1377–1391, 2004.
- Smith, R. B. and Evans, J. P.: Orographic Precipitation and Water Vapor Fractionation over the Southern Andes, *J. Hydrometeorol.*, 8(1), 3–19, doi:10.1175/JHM555.1, 2007.
- Thompson, D. W. J. and Solomon, S.: Interpretation of recent Southern Hemisphere climate change, *Science* (80-. ), 296(5569), 895–899, doi:10.1126/science.1069270, 2002.
- Trenberth, K. E., Fasullo, J. and Smith, L.: Trends and variability in column-integrated atmospheric water vapor, *Clim. Dyn.*, 24(7–8), 741–758, doi:10.1007/s00382-005-0017-4, 2005.
- 10 Vallis, G. K., Zurita-gotor, P., Cairns, C. and Kidston, J.: Response of the Large-Scale Structure of the Atmosphere to Global Warming, *Q. J. R. Meteorol. Soc.*, 141(0000), 1–27, doi:10.1002/qj.2456, 2014.
- Vargas, C. A., Cuevas, L. A., Silva, N., González, H. E., Pol-Holz, D., Narváez, D. A. and others: Influence of Glacier Melting and River Discharges on the Nutrient Distribution and DIC Recycling in the Southern Chilean Patagonia, *J. Geophys. Res. Biogeosciences*, 123(1), 256–270, 2018.
- 15 Viale, M. and Garreaud, R.: Orographic effects of the subtropical and extratropical Andes on upwind precipitating clouds, *J. Geophys. Res. Atmos.*, 120(10), 4962–4974, 2015.
- Viale, M., Houze, R. A., Rasmussen, K. L., Viale, M., Jr., R. A. H. and Rasmussen, K. L.: Upstream Orographic Enhancement of a Narrow Cold-Frontal Rainband Approaching the Andes, *Mon. Weather Rev.*, 141(5), 1708–1730, doi:10.1175/MWR-D-12-00138.1, 2013.
- 20 Waliser, D. and Guan, B.: Extreme winds and precipitation during landfall of atmospheric rivers, *Nat. Geosci.*, 10(3), 179–183, doi:10.1038/ngeo2894, 2017.
- Weidemann, S., Sauter, T., Schneider, L. and Schneider, C.: Impact of two conceptual precipitation downscaling schemes on mass-balance modeling of Gran Campo Nevado ice cap, Patagonia, *J. Glaciol.*, 59(218), 1106–1116, doi:10.3189/2013JoG13J046, 2013.
- 25 Weidemann, S. S., Sauter, T., Kilian, R., Steger, D., Butorovic, N. and Schneider, C.: A 17-year Record of Meteorological Observations Across the Gran Campo Nevado Ice Cap in Southern Patagonia, Chile, Related to Synoptic Weather Types and Climate Modes, *Front. Earth Sci.*, 6, doi:10.3389/feart.2018.00053, 2018a.
- Weidemann, S. S., Sauter, T., Malz, P., Jaña, R., Arigony-Neto, J., Casassa, G. and Schneider, C.: Glacier Mass Changes of Lake-Terminating Grey and Tyndall Glaciers at the Southern Patagonia Icefield Derived From Geodetic Observations and
- 30 Energy and Mass Balance Modeling, *Front. Earth Sci.*, 6, 81, doi:10.3389/feart.2018.00081, 2018b.
- Wentz, F. J., Spencer, R. W., Systems, R. S., Rosa, S. and Hydrology, G.: SSM/I rain retrievals within a unified all-weather ocean algorithm, *J. Atmos. Sci.*, 55(9), 1613–1627, 1998.
- Willis, M. J., Melkonian, A. K., Pritchard, M. E. and Rivera, A.: Ice loss from the Southern Patagonian ice field, South America, between 2000 and 2012, *Geophys. Res. Lett.*, 39(17), 2012.



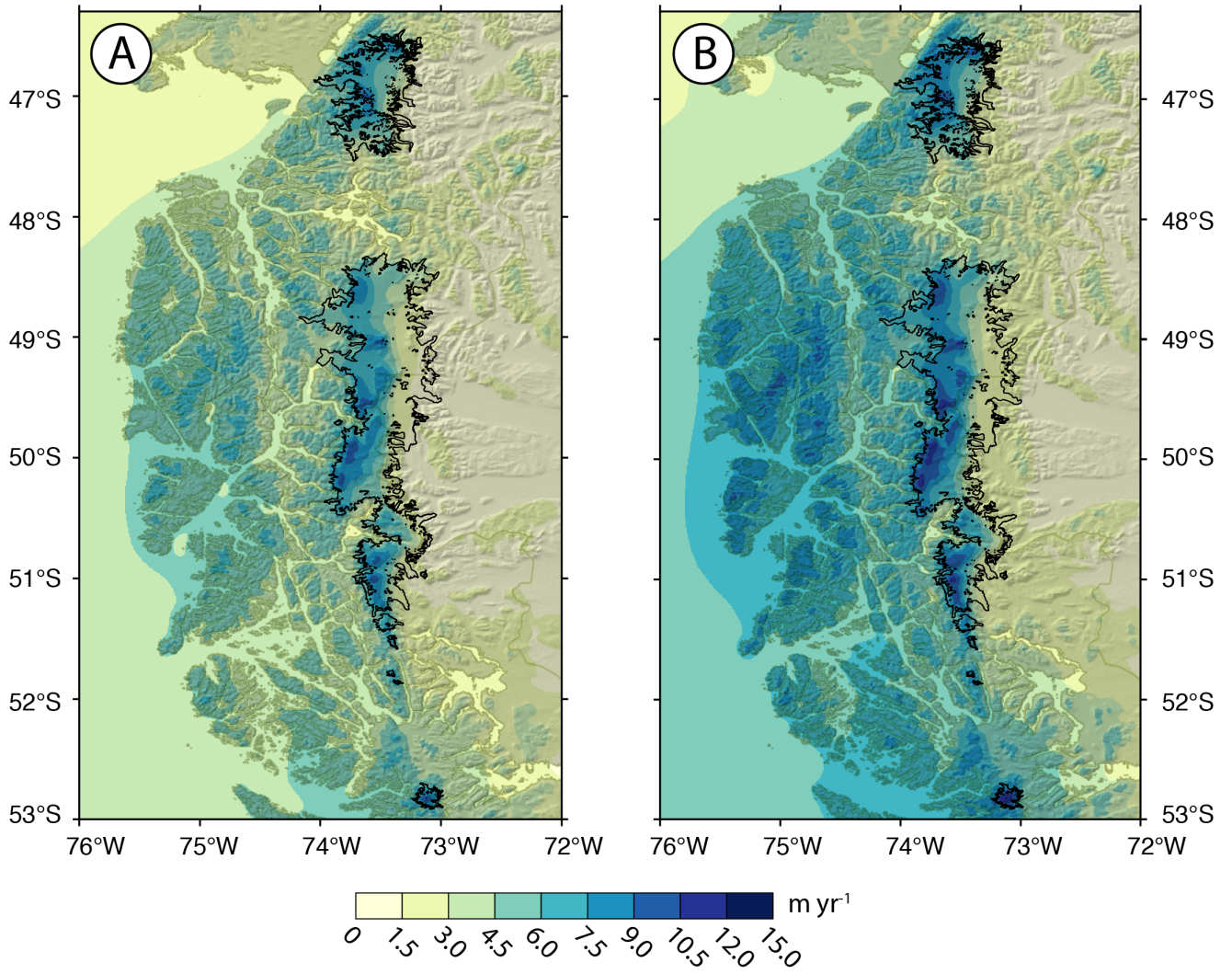


5 **Figure 1:** Precipitation climatology in southern South America. The filled circles indicate precipitation amounts measured by the observational network, established by the Dirección Meteorológica de Chile (DMC), Dirección General de Aguas (DGA), and own weather stations (see Table S1). The colour shaded areas over the ocean shows the rainfall distribution based on the Global Precipitation Measurement (GPM) satellite mission. Black dashed lines roughly delineate the maritime Pre-Cordillera range, Andes main ridge, and the semi-arid Pampa region. Also indicated are the Northern (NPI) and Southern Patagonian Icefields (SPI). The dashed area shows the semi-arid rain-shadow region. Also shown are the simulation (D2) and forcing (D1) domains.



**Figure 2:** Monthly WVF anomalies in Puerto Montt (panel a) and Punta Arenas (panel b). Shown are the running 3-month mean WVF anomalies for the atmospheric soundings and the nearest ERA-Interim grid point from 1990-2016. The blue shaded areas indicate very strong El Niño events ( $\text{ONI} > 1.5$ ). The horizontal blue lines in panel (b) show the mean WVF over water vapor rich and poor phases.

5



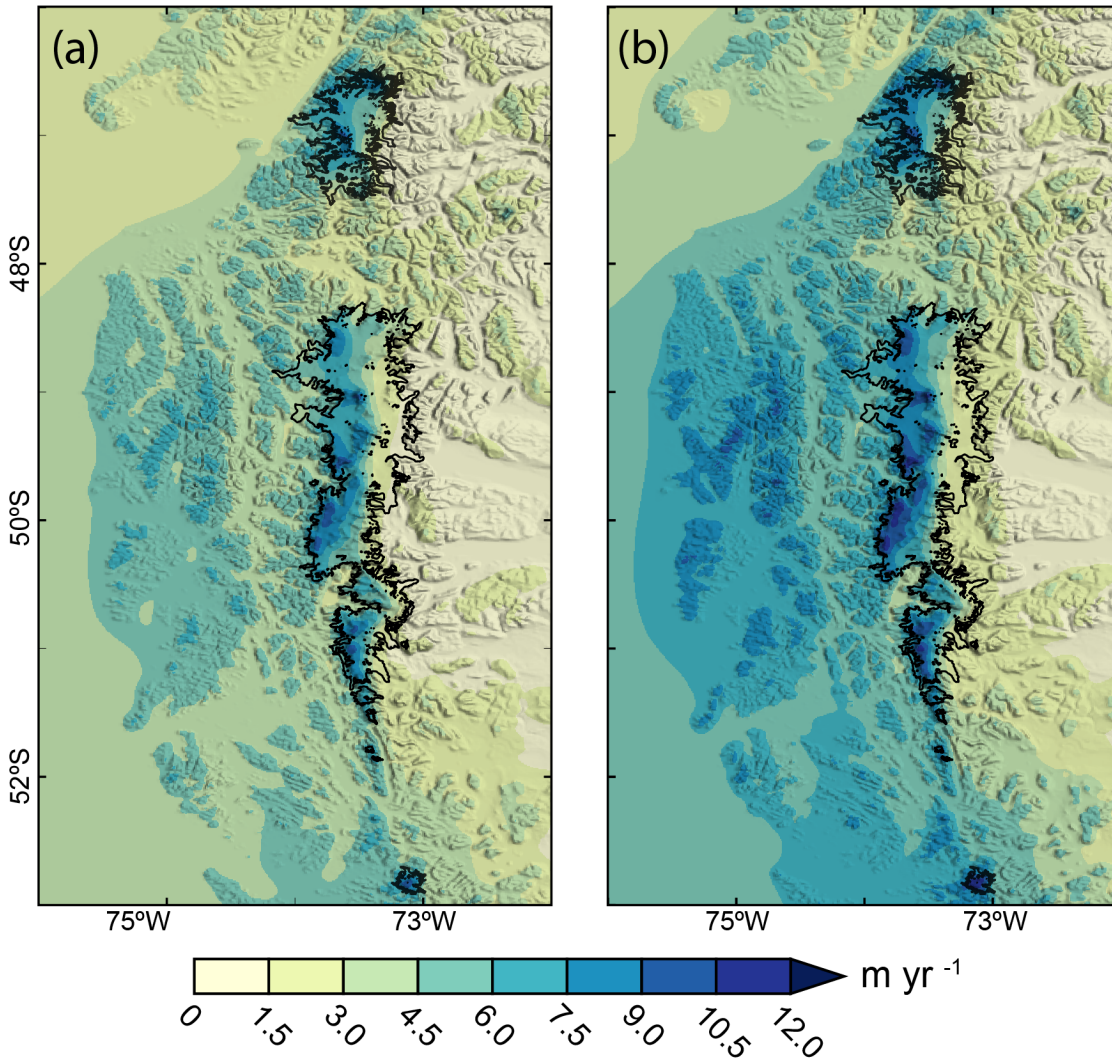


**Figure 3:** Results of the OPM ensemble experiments. Mean precipitation fields (2010-2016) simulated by the OPM using (a) the ‘realistic’ ( $\text{OPM}_{0.45, \text{DR}=0.45}$ ) parameter setup, and (b) the ‘extreme’ ( $\text{OPM}_{0.60}$ ) parameter setup using a DR of 0.6 and the 98th percentile values for the uplift sensitivity factor ( $C_w=0.004$ ) and moist stability frequency ( $N_m=0.007 \text{ s}^{-1}$ ).

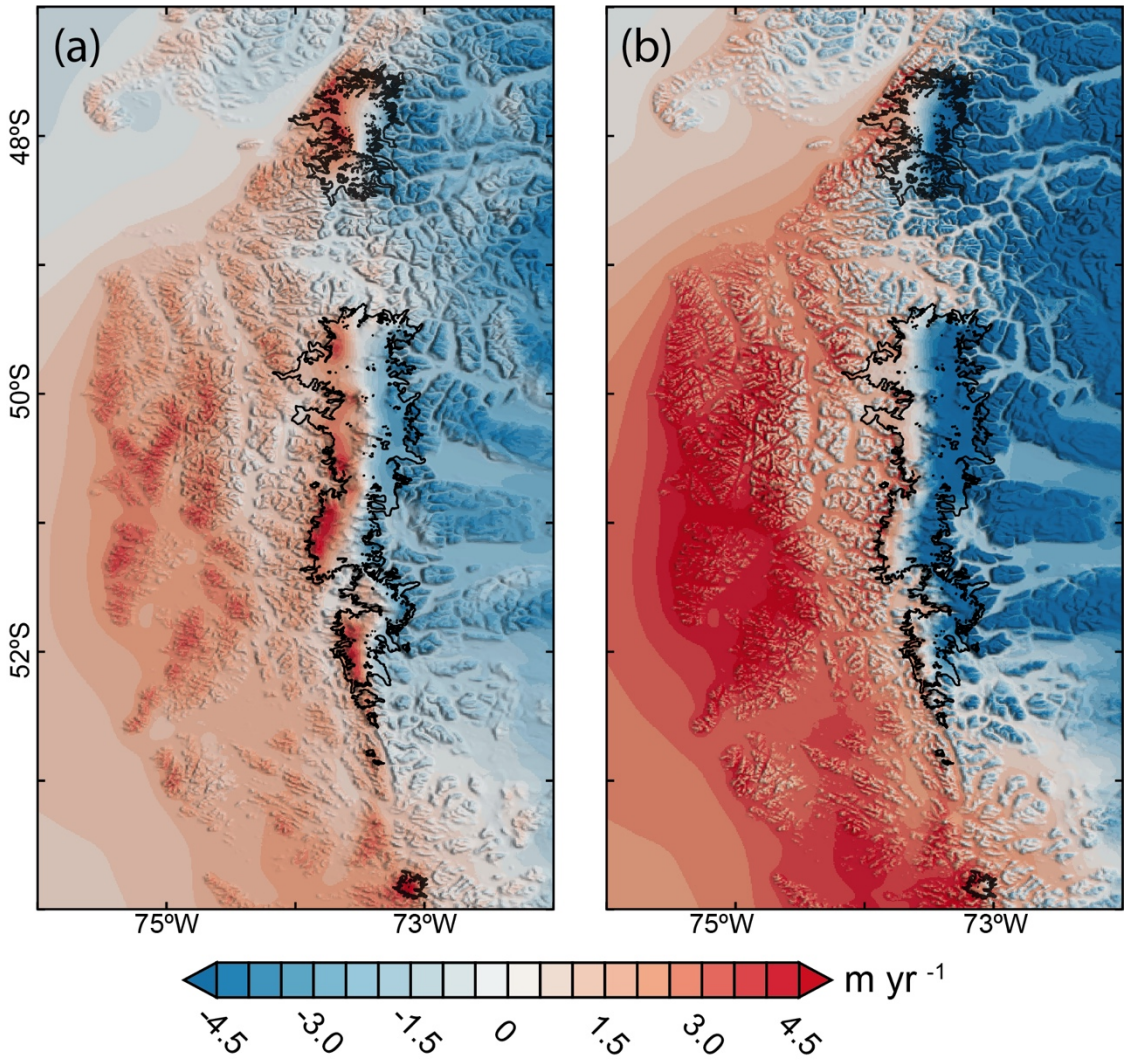


**Figure 4:** Differences between the OPM ensemble experiments and the DR-scaling approach. Panel (a) shows the differences in  $\text{m yr}^{-1}$  between the OPM<sub>0.45</sub> experiments and DRS<sub>0.45</sub> experiment scaling using a DR of 0.45. Similarly, panel (b) shows the differences between OPM<sub>0.60</sub> for the DRS<sub>0.60</sub>.

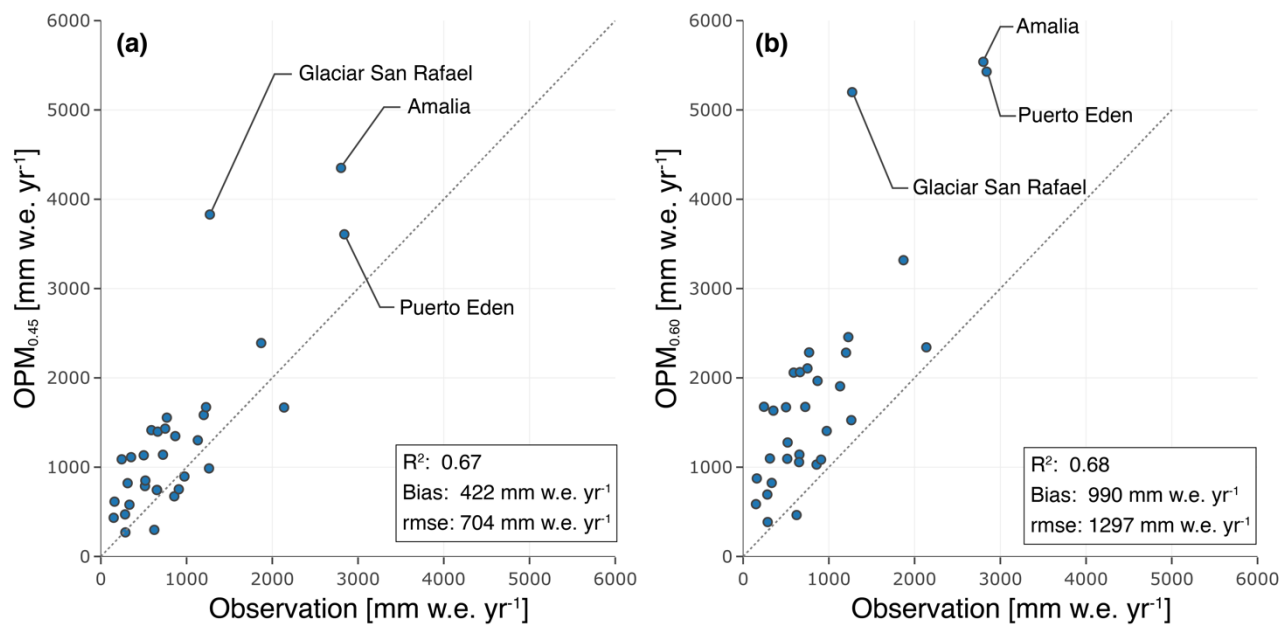


**Figure 5:** Comparison of measured and simulated precipitation for the period 2010-2016. The observations were made by the weather station network of the Dirección Meteorológica de Chile (DMC) and the Dirección General de Aguas (DGA). The only three stations located west of the Patagonian Icefield are labelled.

5

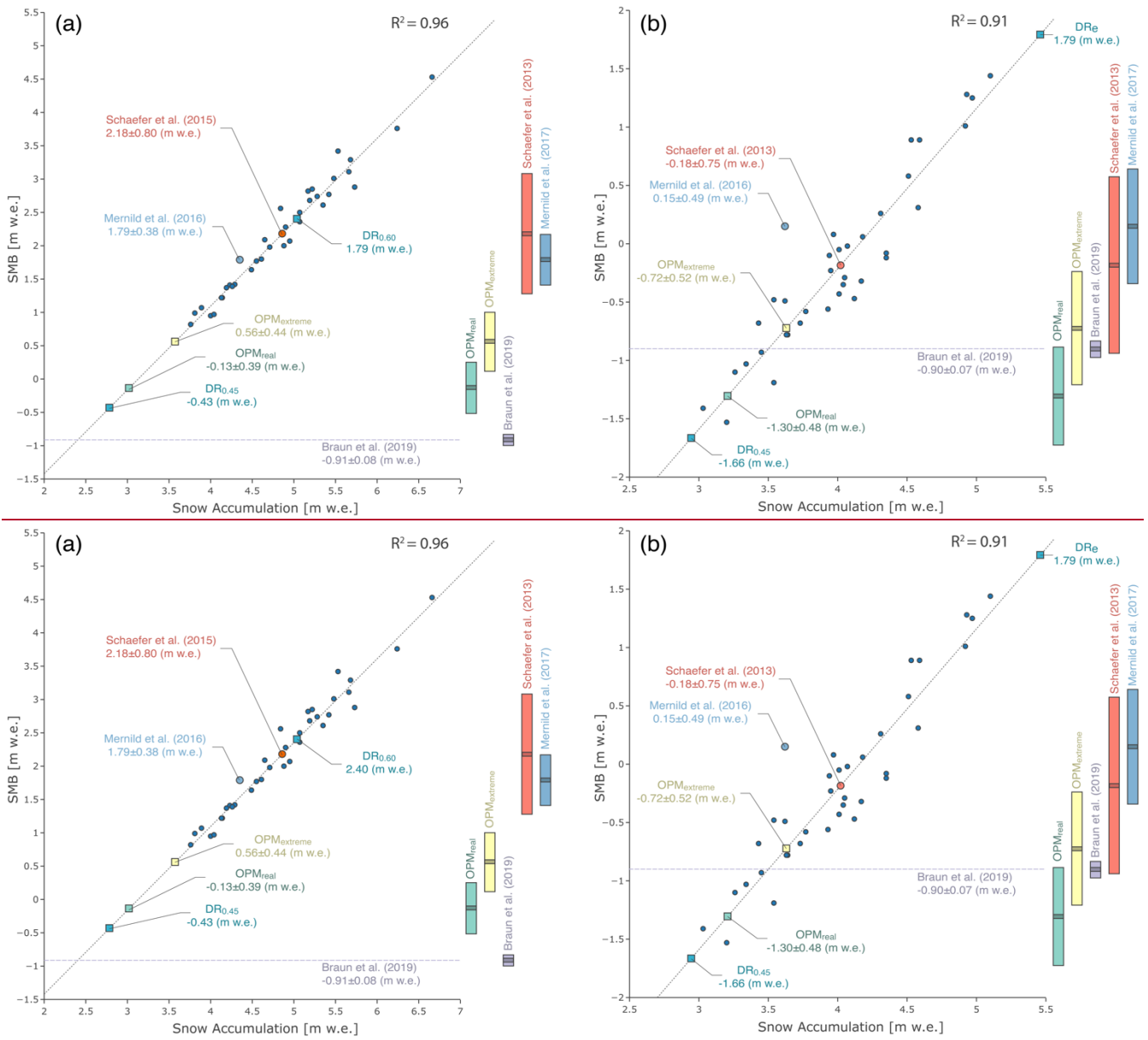
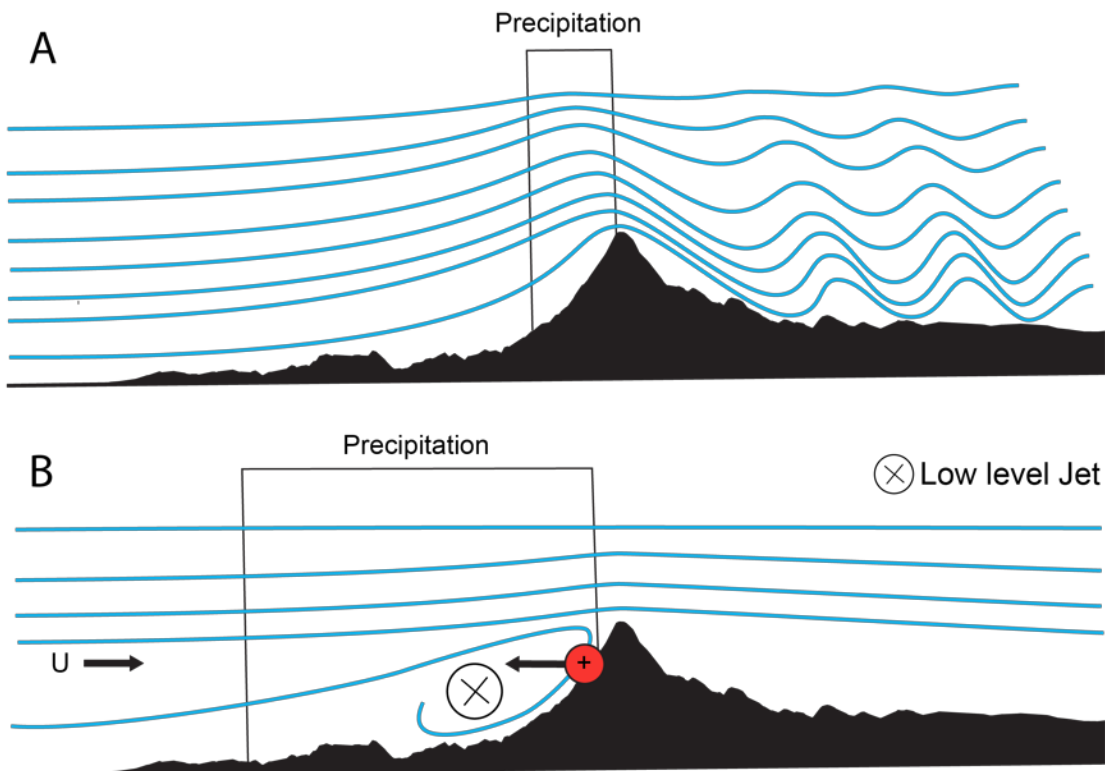


**Figure 65:** Relation between the annual specific accumulation and surface mass balance over the SPI (a) and NPI (b) from 1975-2000. The dark blue dots show the annual SMB values from 1975-2000 for the SPI and NPI estimated by Schaefer et al. (2013) and Schaefer et al. (2015) respectively. The plot also contains the multi-year mean values of Schaefer et al. (2013), Schaefer et al. (2015), Mernild et al. (2017), and the SMB values derived from this study (labelled dots). The dashed grey horizontal lines show the geodetic mass balances obtained from radar interferometry (Braun et al., 2019). The uncertainty of the individual studies is shown on the right side.



5 **Figure 76:** Schematic illustration of the interaction between the atmospheric air flow and the Andes. (A) Linear mountain flow response ( $\hat{H} < 1/H < 1$ ) leads to strong uplift and precipitation along the west slopes. (B) The air flow is blocked by the topography ( $\hat{H} > 1/H > 1$ ) and the resulting pressure gradient (indicated by the red circle) at the west slope slows down the upstream flow. The imbalance between the large-scale pressure gradient and Coriolis-force leads to a northerly low-level jet, which reduces and shifts the uplift motions upstream. This mechanism enhances precipitation in the Pre-Cordillera range, while reducing precipitation at the west slopes of the Andes.

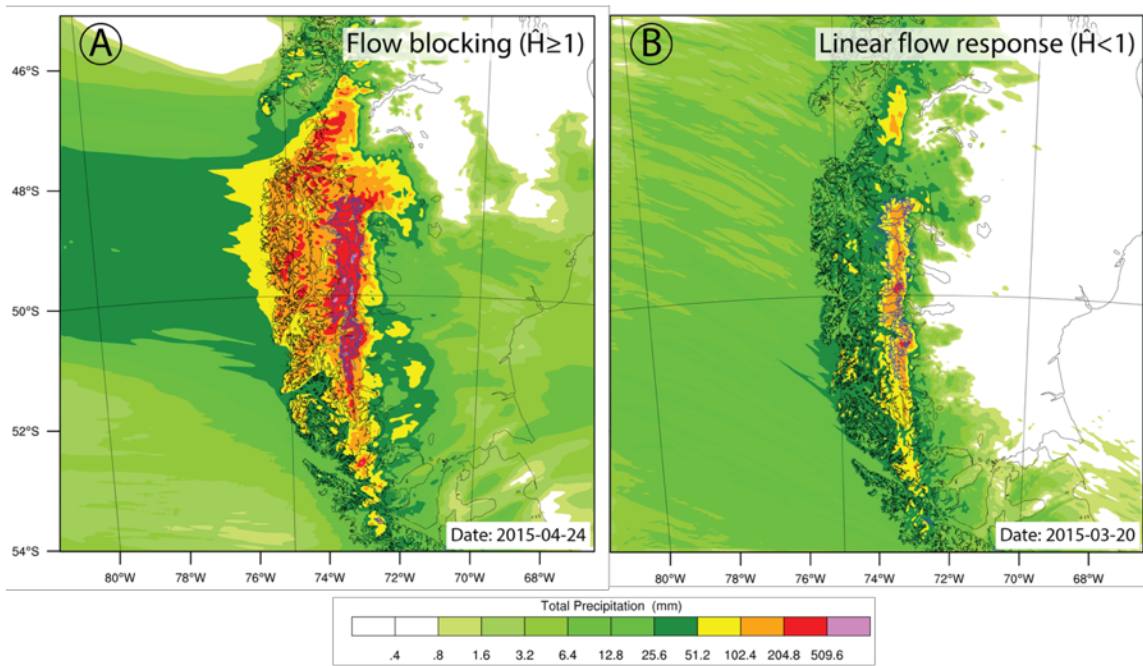


**Figure 876:** Total precipitation sums (3-days) over the SPI and NPI from WRF for different flow regimes. (A) Nonlinear flow response with enhanced precipitation in the Pre-Cordillera range and (B) linear flow response with strong localized precipitation along the west slopes of the Andes.

5

**Table 1:** Comparison of mean precipitation estimates on the SPI and NPI averaged over the entire Icefield and the western (210-330°) and eastern (30-150°) slopes. Values are given in m w.e. yr<sup>-1</sup>. The local maximum values, if available, are shown in parentheses.

	SPI			NPI			Period
	Mean	West	East	Mean	West	East	
<b>Realistic scenario (mean)OPM<sub>0.45</sub></b>	5.06±0.51 (10.09±0.92)	5.93±0.60 (10.09±0.92)	4.06±0.42 (9.92±0.95)	5.38±0.59 (9.43±0.93)	5.83±0.64 (9.43±0.93)	4.37±0.48 (9.30±0.92)	2010-2016
> 3000 m	8.03±0.81	8.60±0.85	8.10±0.82	7.16±0.79	7.40±0.78	6.66±0.73	
2500–3000 m	6.37±0.65	6.93±0.70	6.13±0.63	6.58±0.67	6.84±0.70	5.58±0.53	
2000-2500 m	5.39±0.54	5.70±0.58	4.93±0.50	5.69±0.58	6.20±0.63	5.10±0.52	
1000-2000 m	5.29±0.54	6.13±0.62	4.26±0.44	5.58±0.62	5.77±0.64	4.81±0.53	
< 1000 m	4.26±0.44	5.43±0.56	3.04±0.32	4.81±0.54	5.77±0.64	3.05±0.35	
<b>Extreme scenario (mean)OPM<sub>0.60</sub></b>	5.99±0.59 (11.58±0.98)	7.02±0.68 (11.58±0.98)	4.80±0.49 (11.39±0.99)	6.09±0.64 (10.37±0.96)	6.60±0.69 (10.37±0.96)	4.90±0.53 (10.12±0.95)	2010-2016
> 3000 m	8.89±0.89	9.56±0.94	8.94±0.90	7.67±0.85	7.93±0.85	7.07±0.79	
2500–3000 m	7.09±0.73	7.73±0.78	6.81±0.71	7.05±0.73	7.35±0.75	5.92±0.59	
2000-2500 m	6.08±0.61	6.46±0.65	5.55±0.57	6.16±0.64	6.75±0.69	5.48±0.57	
1000-2000 m	6.19±0.61	7.17±0.70	5.00±0.52	6.21±0.67	6.45±0.70	5.30±0.58	
< 1000 m	5.34±0.53	6.77±0.66	3.84±0.39	5.74±0.58	6.84±0.68	3.72±0.40	
<b>DR<sub>0.45</sub>-scaling (0.45)(mean)</b>	<u>45.6746</u> ( <u>88.06933</u> )	<u>4.66</u> ( <u>7.98</u> )	<u>4.70</u> ( <u>7.95</u> )	<u>45.9460386</u> ( <u>989.6834269</u> )	<u>4.95617</u> ( <u>98.6842</u> )	<u>54.087223</u> ( <u>98.273322</u> )	2010-2016
<b>DR<sub>0.60</sub>-scaling (0.60)</b>	<u>84.4567</u> ( <u>178.710608</u> )	<u>84.416619</u> ( <u>17.49983</u> )	<u>84.537022</u> ( <u>177.40954</u> )	<u>94.1660116</u> ( <u>228.126842</u> )	<u>94.196117</u> ( <u>228.126842</u> )	<u>94.547223</u> ( <u>208.9933322</u> )	<u>2010-2016</u>
<b>Other studies</b>							
Schaefer et al. (2015)	8.36 (>20.0)			8.03±0.37 (>15.0)			1975-2011
Mernild et al. (2017)	8.13±0.32 (>15.0)			6.95±0.34 (>15.0)			1979-2014

---

Lenaerts et al. (2013)	- (>30.0)	- (>30.0)	1979- 2012
Escobar et al. (1992)	7.0	6.7 (over the broad plateau)	1960- 1980

---

# Revisiting extreme precipitation amounts over southern South America and implications for the Patagonian Icefields

Tobias Sauter<sup>1</sup>

5 <sup>1</sup>Climate System Research Group, Institute of Geography, Friedrich-Alexander-University Erlangen-Nürnberg (FAU), Germany

*Correspondence to:* Tobias Sauter (tobias.sauter@fau.de)

## 10 Contents of this file

Figures S1 to S5

Tables S1 to S4

15

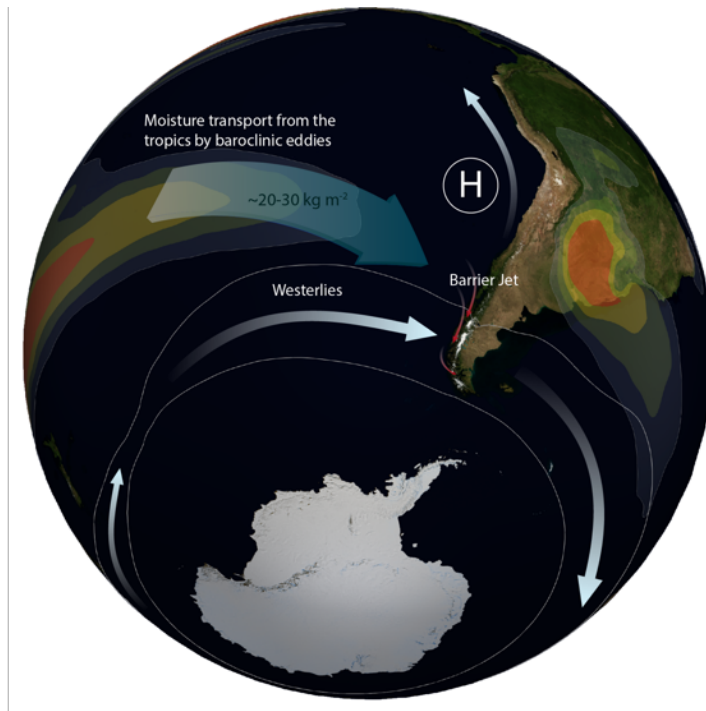


**Figure S1: Schematic illustration of the atmospheric large-scale circulation and moisture transport in the South Pacific. Shown are the location of the westerlies for austral summer (December-January-February), the barrier jet along the Andes (red arrows), and the mean moisture transport by baroclinic eddies (blue shaded arrow). The shading indicates regions of high water vapor variability.**

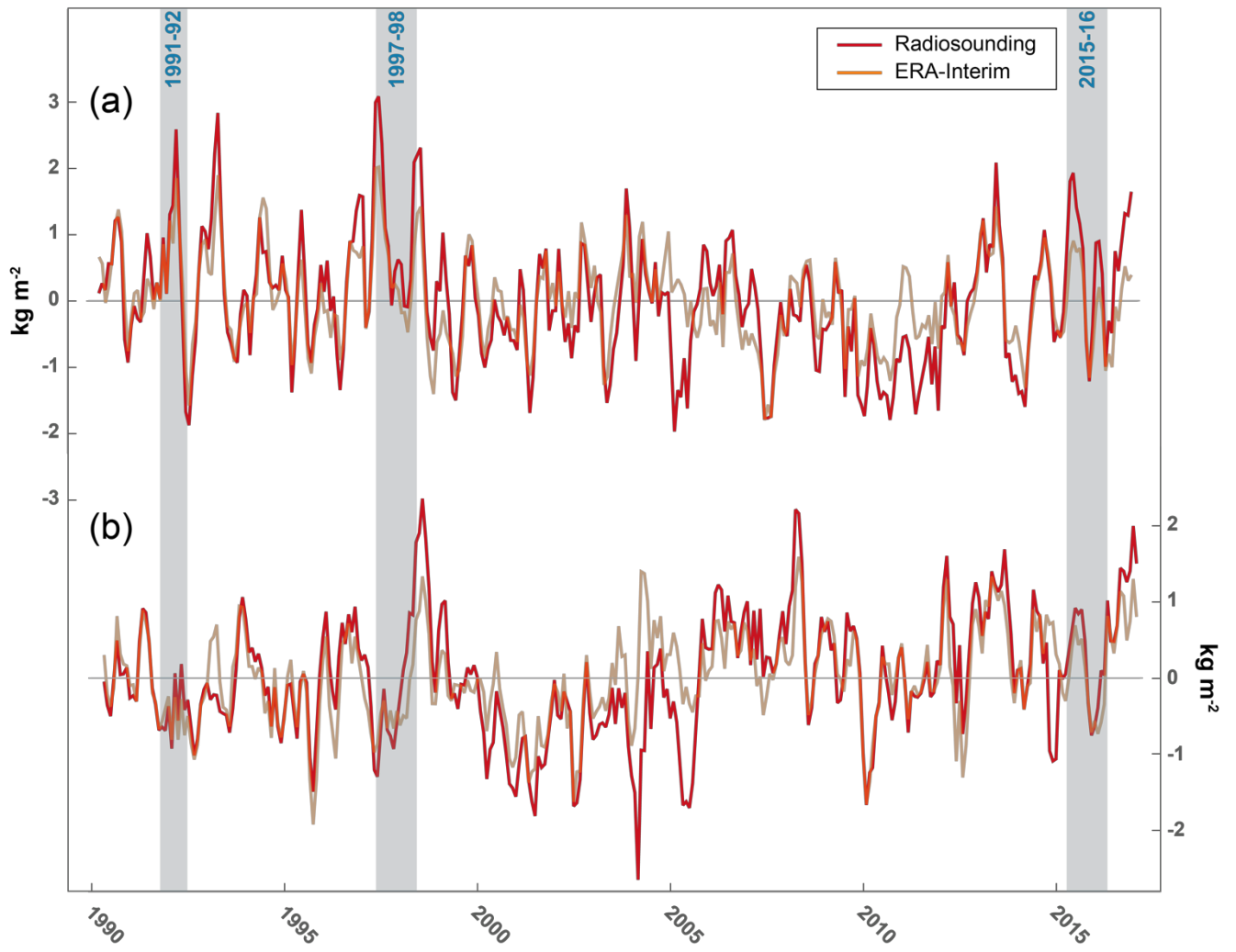
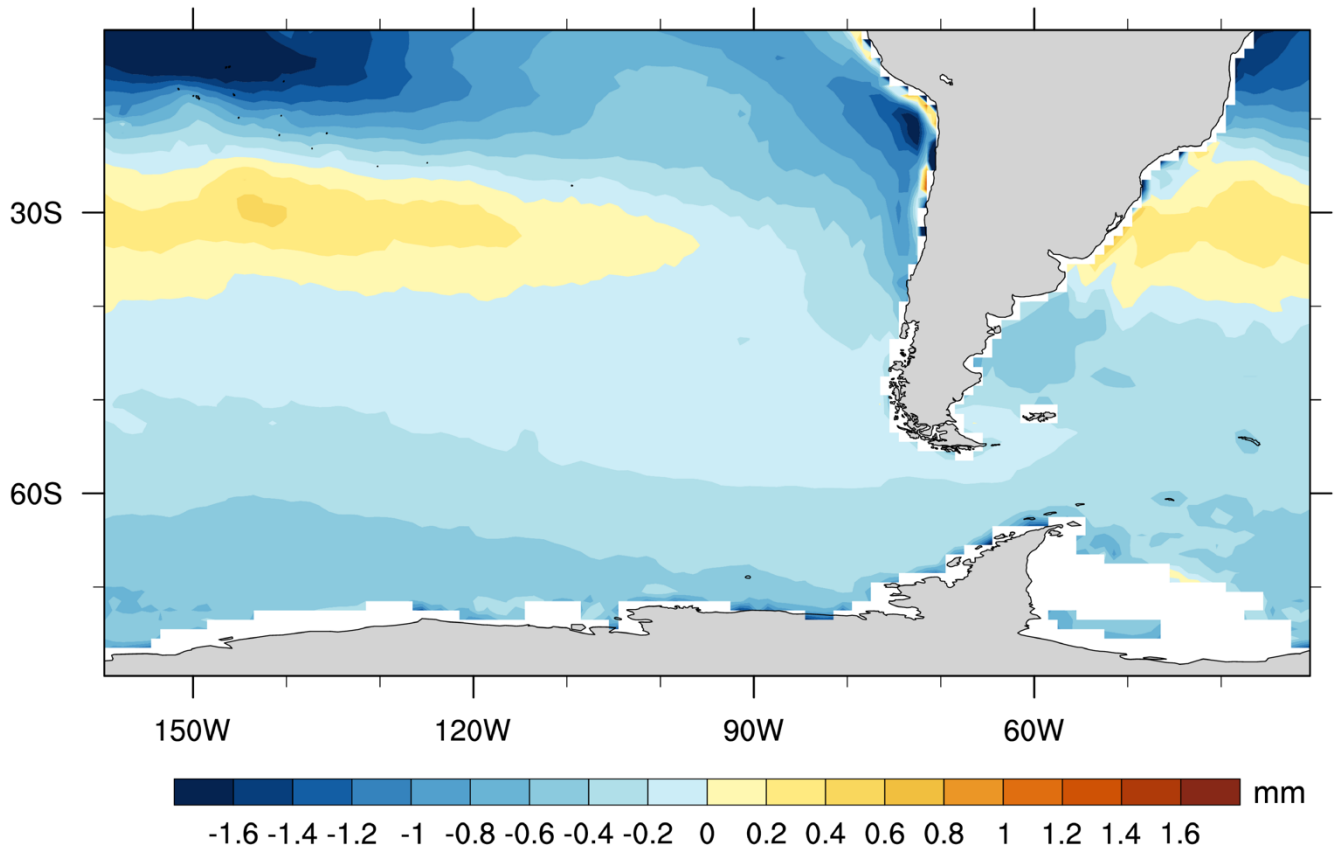


Figure S2: Monthly IWV anomalies in Puerto Montt (panel a) and Punta Arenas (panel b). Shown are the running 3-month mean IWV anomalies for the atmospheric soundings and the nearest ERA-Interim grid point from 1990-2016. The blue shaded areas indicate very strong El Niño events ( $ONI > 1.5$ ).



**Figure S3: Mean differences in the IWV between ERA Interim and SSMI data for the period 1988-2016. Red shading indicates a positive bias in the ERA Interim data.**

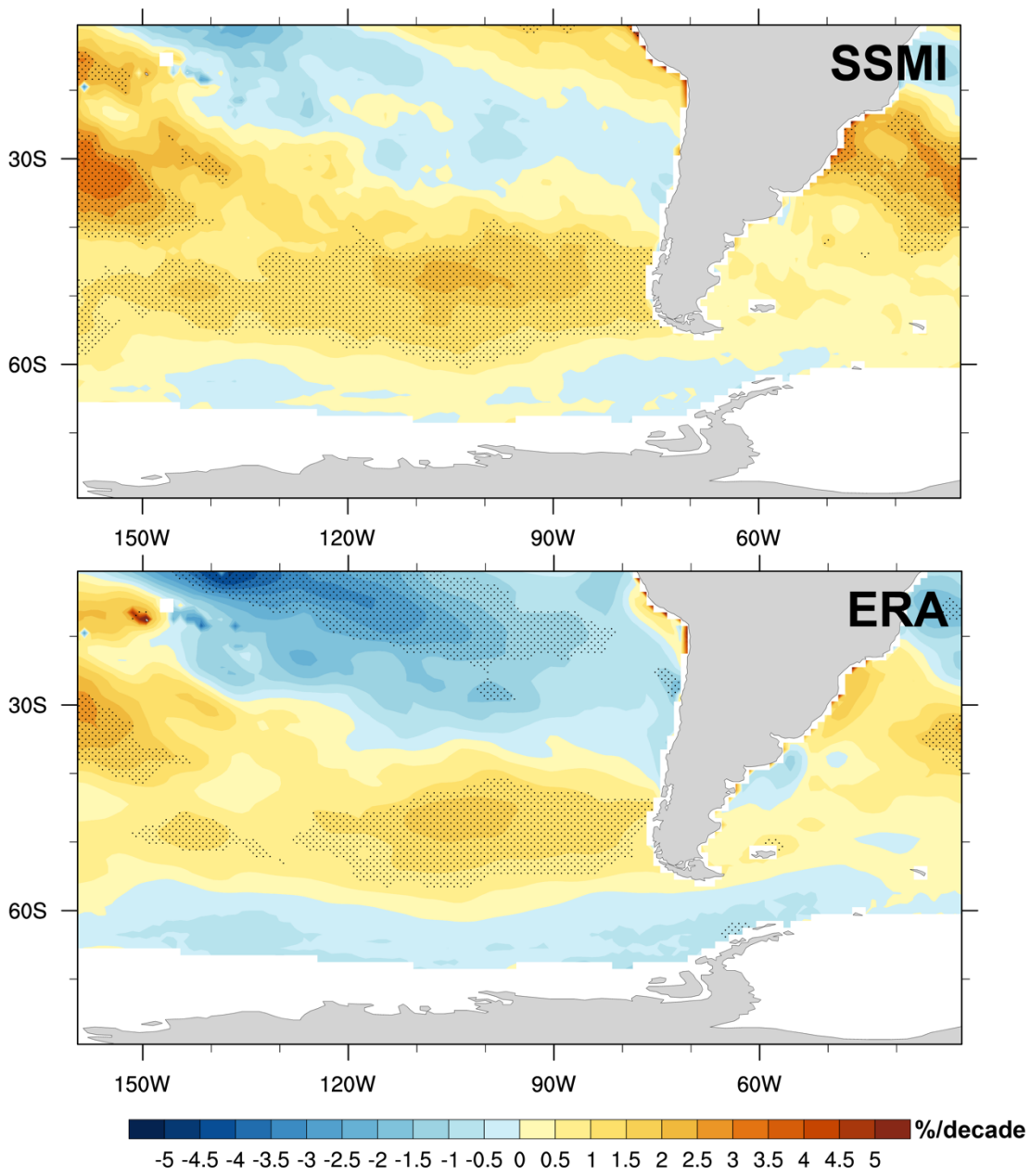
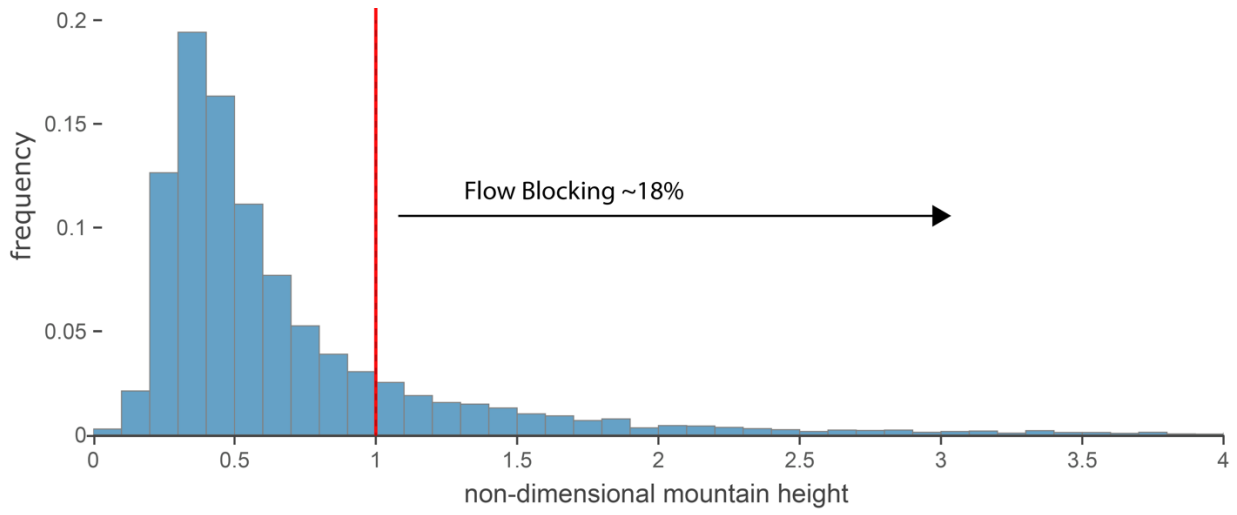


Figure S4: Linear trend of IWV in the SSM/I and ERA-Interim data for the period 1988-2016 (in % per decade). Dotted areas indicate significant long-term trends ( $p < 0.05$ ).



5 **Figure S5: Frequency distribution of the non-dimensional mountain height. The non-dimensional mountain height is calculated from ERA-Interim data (2010-2016) off Patagonia’s west coast (Fig. 1, D1).**

**Table S1. Automatic weather stations in Patagonia. Precipitation sums and trends are given in mm. Bold numbers indicate significant trends ( $p < 0.05$ ).**

Station	Lat	Lon	Sum	Trend in % per decade	from	to
Pirihueico En Pirihueico	-40.02	-71.72	2875	<b>-0.36</b>	1999	2015
El Llolly	-40.07	-72.62	1763	-0.02	1995	2015
Catamutun	-40.17	-73.17	1858	0.02	1998	2015
Venecia	-40.19	-73.43	3964	-0.04	1998	2015
Lago Maihue	-40.22	-72.15	2982	<b>-0.17</b>	1980	2015
Trinidad	-40.31	-73.43	1713	0.13	1998	2015
Lago Ranco	-40.32	-72.47	1923	0.01	1980	2015
Adolfo Matthei	-40.59	-73.11	1256	-0.05	1983	2016
Canal Bajo Osorno Ad.	-40.61	-73.06	1232	-0.04	1980	2016
Anticura	-40.66	-72.18	1185	-0.39	1998	2015
Rio Negro En Chahuilco	-40.71	-73.23	1240	-0.21	2004	2016
Futacuhuin	-40.72	-72.44	1681	-0.07	1995	2015
Rupanco	-40.77	-72.68	1665	-0.04	1994	2015
San Antonio Oeste Aero	-40.78	-65.10	202	<b>0.25</b>	1980	2016
Gobernador Castello	-40.87	-63.00	272	<b>0.21</b>	1980	2016
Purranque	-40.94	-73.14	1309	0.00	1999	2015
Frutillar	-41.13	-73.06	1467	0.00	1994	2015
San Carlos De Bariloche	-41.15	-71.16	589	<b>0.21</b>	1980	2016
Fresia	-41.15	-73.41	1613	-0.03	1994	2015
La Ensenada	-41.23	-72.57	2358	0.00	1980	2005
Maquinchao	-41.25	-68.73	96	0.25	1980	2016
Lago Chapo	-41.42	-72.60	3038	-0.05	1999	2014
El Tepual Puerto Montt Ap.	-41.44	-73.10	1590	-0.05	1980	2016
Puerto Montt	-41.46	-72.94	1845	0.00	1980	2016
Puerto Montt	-41.46	-72.94	1845	0.00	1980	2016
Maullin	-41.62	-73.60	1668	-0.04	1987	2015
Puelo	-41.65	-72.31	2642	-0.17	1997	2016
Ancud 1 (Dga)	-41.86	-73.82	2013	0.12	1993	2015
Hornopiren	-41.94	-72.44	2971	<b>-0.49</b>	1998	2016
El Bolson	-41.94	-71.53	232	<b>1.02</b>	1996	2016
Chepu	-42.05	-73.97	2554	-0.08	1999	2015
Quemchi	-42.14	-73.47	2437	-0.03	2000	2015
Castro 1 (Dga)	-42.46	-73.77	1555	<b>-0.37</b>	1993	2008
Cucao	-42.62	-74.11	2067	0.05	1997	2015
Chaiten	-42.91	-72.71	3408	0.26	1998	2007
Chaiten Ad.	-42.93	-72.70	3590	-0.02	1980	2007
Esquel Aero	-42.93	-71.15	372	<b>0.18</b>	1980	2016
Quellon	-43.11	-73.61	1781	0.01	1993	2015
Puerto. Cardenas	-43.18	-72.43	3922	-0.33	2001	2015
Futaleufu Ad.	-43.19	-71.85	1958	-0.01	1980	2016

Trelew Aero	-43.20	-65.27	171	0.11	1980	2016
Lago Espolon	-43.22	-71.93	2693	-0.13	2001	2015
Valle Rio Frio	-43.47	-72.35	3712	<b>-0.24</b>	2001	2015
Christchurch Intl	-43.49	172.53	486	<b>0.05</b>	1980	2016
Cape Bruny Lighthouse	-43.49	147.15	940	-0.07	1980	2016
Alto Palenaad.	-43.61	-71.81	1589	-0.04	1980	2016
Palena	-43.62	-71.78	1597	<b>-0.20</b>	2001	2015
Maatsuyker Island Lighthouse	-43.66	146.27	1235	<b>-0.16</b>	1980	2016
Marin Balmaceda	-43.77	-72.95	2388	0.17	1994	2015
Paso De Indios	-43.82	-68.88	86	0.44	1980	1996
Chatham Islands Aws	-43.95	-176.57	624	0.16	1994	2011
La Junta	-43.97	-72.41	1998	-0.07	1981	2016
Bordalit	-44.05	-72.32	2508	<b>-0.29</b>	1994	2011
Lago Verde	-44.24	-71.85	1244	0.41	1994	2011
Puerto Puyuhuapi	-44.32	-72.56	2994	-0.08	1981	2015
Rio Cisnes	-44.50	-71.31	273	<b>-0.26</b>	1981	2015
La Tapera	-44.65	-71.67	687	-0.29	1981	2002
Cisnes Medio	-44.67	-72.27	2162	0.00	1982	2015
Puerto Cisnes	-44.73	-72.68	2812	-0.09	1981	2015
Villa Maihuales	-45.17	-72.15	1399	-0.09	1986	2015
Estancia Bao Nuevo	-45.27	-71.53	490	-0.01	2001	2015
Irehuao	-45.27	-71.71	409	0.11	1994	2015
Villa Ortega	-45.37	-71.98	654	-0.14	1981	2015
Puerto Aysen Ad.	-45.40	-72.66	2011	-0.11	1980	2016
Puerto Aysen	-45.40	-72.70	2197	<b>-0.32</b>	1994	2008
El Balseo	-45.40	-72.49	1745	-0.06	1981	2015
Rio Aysen En Puerto Aysen	-45.41	-72.62	1944	0.00	2003	2016
Puerto Chacabuco	-45.46	-72.82	2678	-0.05	1985	2015
Coyhaique Alto	-45.48	-71.60	221	0.02	1985	2016
Coyhaique Conaf	-45.55	-72.06	887	-0.19	2003	2015
Rio Simpson Bajo Junta Coyhaique	-45.55	-72.07	723	-0.24	2006	2016
Coyhaique (Escuela Agricola)	-45.57	-72.03	808	-0.06	1984	2016
Teniente Vidal Coyhaique Ad.	-45.59	-72.11	986	0.03	1980	2016
Comodoro Rivadavia	-45.78	-67.50	203	0.00	1980	2016
Balmaceda Ad.	-45.91	-71.69	529	-0.03	1980	2016
Villa Cerro Castillo	-46.12	-72.15	540	<b>-0.41</b>	1993	2015
Rio Ibaez En Desembocadura	-46.27	-71.99	490	0.26	2006	2016
Puerto Ibaez	-46.29	-71.93	396	<b>0.47</b>	1986	2008
Invercargill Airpor	-46.42	168.33	888	0.01	1980	2016
Alfred Faure (Iles Crozet)	-46.43	51.85	1652	0.02	1980	2016
Bahia Murta	-46.46	-72.67	1208	<b>-0.21</b>	1994	2015
Perito Moreno Arpt	-46.52	-71.02	74	-0.08	1980	2016
Chile Chico	-46.54	-71.71	228	-0.13	1994	2015
Chile Chico Ad.	-46.58	-71.69	255	-0.01	1980	2016
Puerto Guadal	-46.84	-72.70	565	0.31	1994	2015
Marion Island	-46.88	37.87	1857	<b>-0.12</b>	1980	2016

Estancia Valle Chacabuco	-47.12	-72.48	189	-0.29	1994	2015
Rio Baker En Angostura Chacabuco	-47.14	-72.73	745	0.05	2004	2016
Lord Cochrane Ad.	-47.24	-72.59	702	-0.07	1980	2016
Rio Cochrane En Cochrane	-47.25	-72.56	480	0.19	2005	2016
Puerto Deseado	-47.74	-65.90	66	-0.25	1980	2012
Caleta Tortel	-47.80	-73.54	1987	-0.13	2003	2016
Rio Pascua Ante Junta Rio Quetru	-48.16	-73.09	2082	-0.07	2004	2016
Rio Mayer Reten	-48.21	-72.32	200	1.07	1994	2003
Villa Ohiggins	-48.47	-72.56	771	<b>0.36</b>	1994	2008
Lago Ohiggins En Villa Ohiggins	-48.52	-72.60	895	-0.08	2004	2016
Gobernador Gregores	-48.78	-70.17	63	-0.85	1980	1996
Candelario Mancilla	-48.88	-72.74	458	0.05	1994	2016
Puerto Eden	-49.12	-74.41	2346	<b>-0.43</b>	1998	2010
San Julian	-49.31	-67.80	190	0.09	1980	2016
Port-Aux-Francais (Iles Kergu	-49.35	70.25	591	0.02	1980	2016
El Calafate Aero	-50.27	-72.05	145	-0.16	2004	2016
Lago Argentino Arpt	-50.33	-72.30	120	<b>0.98</b>	1980	1999
Enderby Island Aws	-50.48	166.30	737	0.07	1993	2016
Lago Dickson	-50.82	-73.11	910	<b>0.93</b>	2004	2016
Cerro Guido	-50.90	-72.33	265	<b>0.10</b>	1984	2016
Rio Las Chinas En Cerro Guido	-51.05	-72.52	226	0.29	2005	2016
Torres Del Paine	-51.18	-72.97	739	0.04	1983	2016
Cerro Castillo	-51.26	-72.33	315	0.00	1981	2016
Rio Gallegos Aero	-51.62	-69.28	214	<b>0.19</b>	1980	2016
Teniente Gallardo Puerto Natales Ad.	-51.67	-72.53	192	<b>1.69</b>	1999	2016
Casas Viejas	-51.70	-72.33	256	<b>0.24</b>	1981	2015
Puerto Natales	-51.73	-72.48	490	-0.02	1986	2016
Mount Pleasant	-51.82	-58.45	471	0.03	1992	2016
Rio Rubens En Ruta N 9	-52.03	-71.94	414	<b>-1.29</b>	2007	2016
Teniente Merino	-52.03	-70.73	221	0.09	1984	2015
Rubens En Ruta N. 9	-52.04	-71.94	473	<b>-0.52</b>	1990	2005
Rio Penitente En Morro Chico	-52.05	-71.42	265	-0.15	2007	2016
Monte Aymond	-52.16	-69.61	250	-0.03	1996	2016
Villa Tehuelche	-52.44	-71.40	337	-0.04	1981	2016
Rio Perez	-52.55	-71.96	525	-0.04	1990	2014
Campbell Island Aws	-52.55	169.17	1017	<b>0.44</b>	1996	2016
Seno Skyring	-52.55	-71.96	584	-0.56	2002	2016
San Gregorio	-52.57	-70.07	264	-0.03	1992	2016
Rio Verde	-52.60	-71.50	337	0.02	1994	2016
Rocallosas	-52.65	-71.96	327	<b>-0.88</b>	1994	2015
Cerro Sombrero	-52.78	-69.29	248	-0.06	1984	2014
Bahamondes	-52.80	-72.93	3367	<b>-0.75</b>	2000	2015
Bahia San Felipe	-52.87	-69.93	351	0.12	1980	2016
Isla Riesco	-52.88	-71.57	408	-0.09	1991	2015
Punta Arenas	-53.12	-70.88	923	0.02	1980	2016
Canal De Trasvase Estero Llau-Llau	-53.13	-70.94	648	-0.10	2005	2016

Rio Las Minas En Bt. Sendos	-53.14	-70.99	780	-0.03	2000	2016
Las Minas	-53.14	-70.98	774	-0.14	1996	2015
Laguna Lynch	-53.14	-70.98	435	-0.04	1980	2015
Fuentes Martinez Porvenir Ad.	-53.19	-70.32	260	-0.03	1986	2016
Porvenir	-53.29	-70.37	315	<b>-0.20</b>	1991	2015
Onaisin En Maria Cristina	-53.31	-69.27	315	-0.12	1990	2016
San Sebastian	-53.32	-68.66	294	0.13	1990	2016
Lago Parrillar	-53.40	-71.25	800	0.00	1990	2016
Cameron	-53.64	-69.65	366	0.08	1994	2016
San Juan	-53.65	-70.96	544	<b>0.29</b>	1980	2016
Russfin	-53.76	-69.19	429	-0.01	1994	2016
Rio Caleta En Tierra Del Fuego	-53.86	-70.00	340	-0.15	2007	2016
Rio Grande En Tierra Del Fuego	-53.89	-68.88	276	0.14	2007	2016
Seccion Rio Grande	-53.90	-68.92	401	0.15	1991	2011
Pampa Huanaco	-54.05	-68.80	340	<b>0.28</b>	1994	2016
Macquarie Island	-54.50	158.94	912	-0.03	1980	2016
Ushuaia Malvinas Argentinas	-54.84	-68.30	335	0.24	1980	2016
Guardia Marina Zanartu Pto Williams	-54.93	-67.62	466	-0.09	1980	2016
Rio Robalo En Puerto Williams	-54.95	-67.64	389	0.14	2005	2016

5 **Table S2. Comparison of the IWV trends between atmospheric soundings and the nearest ERA-Interim grid point. Numbers are given in mm decade<sup>-1</sup>. Bold numbers indicate significant trends (p<0.05).**

	1988-2016	1988-2009	2010-2016
<b>Puerto Montt</b>			
Radiosounding	-0.22 (-1.5%)	-0.42 (-3.0%)	2.87 (19.4%)
ERA-Interim	-0.16 (-1.3%)	-0.25 (-2.0%)	0.65 (5.2%)
<b>Punta Arenas</b>			
Radiosounding	0.23 (2.2%)	0.07 (0.6%)	1.23 (11.3%)
ERA-Interim	0.14 (1.3%)	0.05 (0.4%)	0.80 (7.0%)

10 **Table S3. Comparison of the OPM<sub>0.45</sub> and OPM<sub>0.60</sub> experiments (DR=0.45) with observations. Given are the latitude (lat), longitude (lon), altitude (alt), the precipitation values from the orographic precipitation model experiments (OPM<sub>0.45</sub> and OPM<sub>0.60</sub>) and the observations (Obs) at the weather stations. The precipitation values are given in mm yr<sup>-1</sup>.**

Location	lat	lon	alt	OPM <sub>0.45</sub> (0.45)	OPM <sub>0.60</sub> (0.6)	Obs
Villa Cerro Castillo	-46.12	-72.15	345	471	693	282
Rio Ibaez En Desembocadura	-46.26	-71.99	220	298	463	623
Bahia Murta	-46.46	-72.66	240	849	1275	1017
Lago General Carrera Fachinal	-46.54	-72.22	18	579	823	333
Glaciar San Rafael	-46.64	-73.85	8	3829	5198	1271
Puerto Guadal	-46.84	-72.70	210	745	1141	656

Estancia Valle Chacabuco	-47.11	-72.48	343	613	874	159
Rio Nef Antes Junta Estero El Revalse	-47.13	-73.08	281	895	1405	974
Rio Baker En Angostura Chacabuco	-47.14	-72.72	160	673	1029	856
Lago Cachet 2 En Glaciar Colonia	-47.19	-73.25	427	1088	1676	243
Lord Cochrane Ad.	-47.24	-72.58	204	744	1056	652
Rio Cochrane En Cochrane	-47.25	-72.56	140	788	1094	514
Rio Colonia En Nacimiento	-47.33	-73.11	146	986	1526	1261
Caleta Tortel	-47.79	-73.53	10	2389	3318	1870
Rio Pascua Ante Junta Rio Quetru	-48.15	-73.08	20	1668	2342	2137
Lago Ohiggins En Villa Ohiggins	-48.51	-72.59	300	752	1084	909
Candelario Mancilla	-48.87	-72.73	300	850	1276	519
Rio Punta Eva En Puerto Eden	-49.11	-74.41	10	3607	5429	2840
El Calafate Aero	-50.26	-72.05	204	433	586	149
Lago Dickson	-50.82	-73.11	200	1301	1906	1130
Lago Paine	-50.84	-72.90	440	1132	1671	500
Cerro Guido	-50.89	-72.33	230	820	1097	312
Amalia	-50.95	-73.69	0	4350	5539	2801
Rio Paine En Parque Nacional 2	-50.96	-72.79	90	1139	1675	724
Nunatak Grey	-50.97	-73.22	300	1414	2059	589
Lago Sarmiento	-51.01	-72.71	110	1111	1633	352
Lago Pehoe	-51.07	-72.99	40	1347	1966	868
Lago Grey	-51.11	-73.13	50	1397	2064	663
Glaciar Tindall	-51.11	-73.28	345	1584	2282	1200
Torres Del Paine	-51.18	-72.96	25	1431	2106	750
Rio Rincon En Ruta Y-290	-51.31	-72.82	36	1554	2285	769
Rio Serrano En Desembocadura	-51.33	-73.10	25	1671	2456	1227

**Table S4. Summary of the WRF configuration.**

	Value
<b>Domain configuration</b>	
Horizontal grid spacing	12.5-km, 2.5-km, and 500-m
Vertical levels	55
Model top pressure	100 hPa
<b>Model physics</b>	
Radiation	RRTMG
Microphysics	Morrison
Cumulus	Kain-Fritsch
Planetary boundary layer	MYNN Level 2.5
Atmospheric surface layer	Monin Obukhov

---

Land surface	Noah-MP	
Top boundary condition	Rayleigh damping	
<b>Lateral boundaries</b>		5
Forcing	ERA-Interim 0.75°x0.75°, 6-hourly	

---